ORIGINAL ARTICLE

Petrochronology of high-pressure granulite facies rocks from Southern Brasília Orogen, SE Brazil: Combining quantitative compositional mapping, single-element thermometry and geochronology

Regiane Andrade Fumes[1] | George Luiz Luvizotto[1] | Renato Moraes[2] |
Pierre Lanari[3] | Claudio de Morisson Valeriano[4] | Thomas Zack[5] |
Mark J. Caddick[6] | Luiz Sergio Amarante Simões[1]

[1]Department of Geology, São Paulo State University, Rio Claro, Brazil

[2]Department of Mineralogy and Geotectonics, University of São Paulo, São Paulo, Brazil

[3]Institute of Geological Sciences, University of Bern, Bern, Switzerland

[4]TEKTOS Research Group, Faculdade de Geologia, Universidade do Estado Rio de Janeiro (UERJ), Rio de Janeiro, Brazil

[5]Department of Earth Sciences, University of Gothenburg, Gothenburg, Sweden

[6]Department of Geosciences, Virginia Tech, Blacksburg, Virginia, USA

Correspondence
Regiane Andrade Fumes, Department of Geology, São Paulo State University, Av. 24A, 1515, Rio Claro 13506-900, Brazil.
Email: regiane.fumes@unesp.br

Funding information
National Council for Scientific and Technological Development (Conselho Nacional de Desenvolvimento Científico e Tecnológico), Grant/Award Numbers: 141604/2018-2, 311606/2019-9, 305720/2001-1, 486328/2013-9; Coordination of Superior Level Staff Improvement (Coordenação de Aperfeiçoamento de Pessoal de Nível Superior), Grant/Award Number: Finance Code 001; São Paulo Research Foundation (Fundação de Amparo à Pesquisa do Estado de São Paulo), Grant/Award Numbers: 2016/22627-3, 2015/05230-0

Abstract

We use a combination of several in situ techniques to assess the *P-T*-t path of high-pressure granulites from the Passos Nappe in the Southern Brasília Orogen (SE Brazil). Quantitative element mapping and single-element thermometers (Zr-in-rutile and Ti-in-quartz) are coupled with *P-T* pseudosections and monazite and rutile dating. Compositional and temperature maps, based on cathodoluminescence mapping and in situ analyses of Ti-in-quartz, are presented as a novel approach to evaluate crystallization temperature. The studied rocks have a pelitic protolith and record a peak pressure assemblage of garnet + kyanite + rutile + K-feldspar + quartz + melt ± plagioclase that formed at ~830°C and 1.2 GPa. Retrograde conditions of ~560°C and 0.6 GPa are determined based on the grossular content of garnet and the crystallization of biotite and ilmenite. Metamorphic peak conditions occurred ca. 635 Ma, according to monazite dating, with a younger date of ca. 615 Ma associated with later kyanite crystallization. Rutile ages of ca. 590 Ma are linked to the late retrograde stage (at ~600°C). Results show that the distribution of Ti-in-quartz is heterogeneous, decreasing in abundance towards the rim of crystals, though the higher temperatures constrained with Ti-in-quartz thermometry are broadly consistent with peak conditions. The peak pressure conditions are consistent with continental collision setting in the Southern Brasília Orogen and were followed by an early cooling/decompression stage and then by a slow cooling during exhumation and transport to shallower crustal levels.

KEYWORDS
cathodoluminescence, phase equilibrium modeling (THERMOCALC), *P-T*-t path, single element thermometers, Western Gondwana, XMapTools

1 | INTRODUCTION

High-pressure granulites are key markers of geodynamic processes in overthickened or subducted continental crust (O'Brien, 2008), recording extreme pressure (*P*), and temperature (*T*) conditions of crustal metamorphism. They enable us to access information about the roots of orogenic belts, where continental crust could be deeply buried, and are commonly exposed in deeply eroded Precambrian orogens, such as the Brasília Orogen (SE Brazil).

The reconstruction of *P-T*-time (t) paths of high-pressure granulites contributes significantly to our understanding of the evolution of collisional orogenic belts. The metamorphic evolution of such rocks is often complex and should not generally be viewed as the result of a single phase of equilibration under granulite facies conditions (O'Brien & Rötzler, 2003). Many factors are involved in their genesis and control their evolution, including burial and exhumation rates, crustal heat budgets, contrasting intra- and inter-crystalline diffusion rates of the range of conditions involved, and the role of melt and fluids in metamorphic equilibration and deformation. Each of these parameters can be reflected in the results of geochronology and mineral thermobarometry, though the metamorphic record of each process is often difficult to read.

Trace element geothermometers are especially useful for high-pressure granulites because, in general, garnet is the only Fe-Mg phase in rocks with pelitic protoliths, so conventional exchange thermometry is not possible. In recent decades, single element geothermometers, such as Ti-in-quartz and Zr-in-rutile, have become important tools for calculating crystallization *T* in metamorphic rocks (e.g., Ashley & Law, 2015; Cruz-Uribe et al. (2018); Kendrick & Indares, 2018a; Pape et al., 2016; Pauly et al., 2016; Taylor-Jones & Powell, 2015; Thomas et al., 2010, 2015) since they are also generally considered less prone to post-peak resetting than, for example, Fe-Mg thermometers. Ti-in-quartz and Zr-in-rutile equilibria are also affected by pressure, so that if quartz and rutile are in equilibrium, it is possible to extract both *P* and *T* information (Thomas et al., 2010). Trace element thermometers are, therefore, useful for interpreting *P-T*-t paths and are complementary to other approaches.

In high-grade rocks such as high-pressure granulites, Ti-in-quartz and Zr-in-rutile contents commonly show a large spread (e.g., Kendrick & Indares, 2018a; Pape et al., 2016; Taylor-Jones & Powell, 2015). Cathodoluminescence (CL) mapping is a valuable tool to study the Ti distribution in quartz and its correlation with rock texture since CL emission in quartz (captured using a blue filter) has been shown to be proportional to its Ti content (Kendrick & Indares, 2018a; Leeman et al., 2012). The ability to produce standardized maps (i.e., quantitative maps, e.g., Lanari et al., 2019) by co-processing qualitative CL maps and quantitative analyses raises the possibility of recovering detailed records of *T* conditions using the Ti-in-quartz thermometry, though this is still an emerging line of research.

Besides the importance of constraining the *P-T* evolution of high-grade rocks, it is also necessary to constrain on the relationship between the *P-T* conditions and age of this metamorphism and use geochronology to help place rocks within an appropriate regional tectonic context. The application of U-Pb (Th) geochronology techniques to assess accurate and precise ages of accessory minerals such as monazite and rutile has become particularly useful for deciphering the tectonic history of orogenic belts (Armstrong, 1991; Dickin, 1995; Gebauer & Grünenfelder, 1979), and detailed petrochronology is becoming widespread in the many cases where multiple stages of the *P-T*-t path are be recorded (Engi et al., 2017; Foster et al., 2004). The ages of prograde heating, thermal peak conditions, and retrograde stages of metamorphism can be recorded in monazite (e.g., Prent et al., 2019; Reno et al., 2012; Rocha et al., 2017; Tiwari & Biswal, 2019), whereas rutile is potentially the most suitable mineral for studying the influence of intragrain and intergrain ion diffusion during cooling (Zack & Kooijman, 2017). Combining ages from coexisting minerals is a powerful tool for uncovering complex metamorphic histories and constraining the cooling rates and thermal evolution of high-grade rocks.

The aim of this work is to present *P-T* data and ages of metamorphic processes on high-pressure granulites from the Passos Nappe, showing how a combination of tools, namely, mineral analysis, element mapping, thermodynamic modeling, single element thermometry, and in situ dating, can be used to assess a detailed *P-T*-t path of these rocks. Furthermore, we discuss tectonic settings of the Passos Nappe and discuss possible correlation between the high-pressure granulite and similar rocks that occur further south in the Andrelândia Nappe System.

2 | GEOLOGICAL SETTING

2.1 | Regional Setting

The Neoproterozoic Brasília Orogen (Figure 1) is located in central/southeastern Brazil, where it borders the western and southern margin of the São Francisco Craton. Its development is related to the early assembly of West

Gondwana (Dardenne, 2000; Valeriano, Machado, et al., 2004, Valeriano et al., 2008; Valeriano, 2017; Figure 1a). The Southern Brasília Orogen, the portion of the orogen that occurs to the south of the Pirineus Syntaxis (Figure 1b) (Araújo Filho, 2000), is divided, based on rock types and their tectonic setting, into four tectonic domains (Fuck et al., 1994). From east to west and from bottom to structural top, these are (i) the Cratonic Zone and its sedimentary cover; (ii) the External (foreland) Zone that represents the low-grade metamorphic fold-and-thrust belt of the orogen; (iii) the Internal Zone, comprising the tectonically overlying nappes of high-grade metamorphic rocks; (iv) and the Goiás

magmatic arc zone. This division is broadly accepted in the literature (Dardenne, 2000; Pimentel, 2016; Valeriano, 2017; Valeriano, Dardene, et al., 2004; Valeriano et al., 2008). The rocks from the Brasília Orogen record a complete Wilson Cycle, starting in the Tonian (ca. 0.9 Ga) with rifting and the development of a passive margin and opening of the Goianides ocean, followed by subduction of distal continental margin units (ca. 0.63 Ga) and ending with nappe stacking and exhumation between ca. 610 and 580 Ma in a continental collision setting (Fuck et al., 2017; Tedeschi et al., 2018; Valeriano, 2017; Valeriano et al., 2000, 2008).
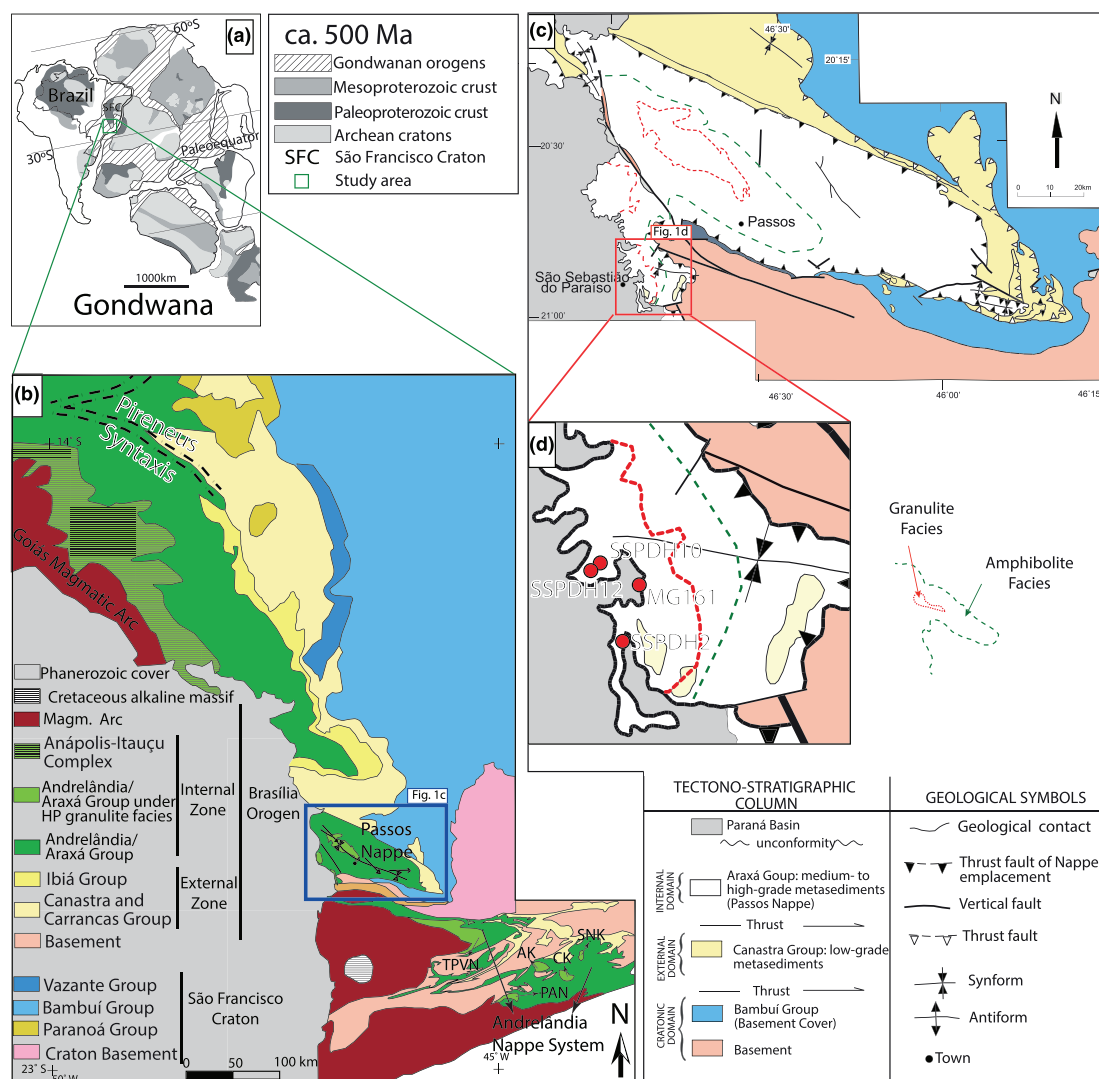

FIGURE 1 Geological setting of the study area. (a) Gondwana map (ca. 500 Ma) showing the location of the study area (green rectangle), after Spencer et al. (2013). (b) Tectonic map of the Southern Brasília Orogen and adjoining southwestern margin of the São Francisco craton modified from Valeriano (2017) and Campos Neto et al. (2010). TPVN, Três Pontas-Varginha Nappe; SNK, Serra da Natureza Klippe; CK, Carvalhos Klippe; PAN, Pouso Alegre Nappe; and AK, Aiuruoca Klippe. (c) Geological map of the Passos Nappe (updated from Valeriano, Machado, et al., 2004). (d) Detail of the map in the southwest of the Passos Nappe with sample location [Colour figure can be viewed at wileyonlinelibrary.com]

Most of the rocks of the Internal Zone belong to the Araxá Group (Barbosa, 1955; Seer & Dardenne, 2000; Seer et al., 2001; Valeriano, Dardene, et al., 2004, Valeriano, Machado, et al., 2004; Valeriano, 2017), exposed in a series of nappes, such as the Passos Nappe, from where the studied samples derive. The rocks of Araxá Group in the southernmost portion of the Southern Brasília Orogen have been compared by Trouw et al. (1984) to those of the Andrelândia Group, which occur further south and have similar lithology and metamorphic conditions.

2.2 | Lithostratigraphy and tectonic setting

The Passos Nappe is predominantly composed of metasedimentary rocks (Figure 1c), traditionally included in the Araxá Group (Simões, 1995; Valeriano, Machado, et al., 2004), with minor lenses of tholeiitic metabasic rocks. The basal units of the nappe contain biotite-muscovite schist, marble, and minor muscovite quartzite. These rocks are overlain by a thick package of muscovite-rich quartzite followed by fine grained muscovite-biotite gneiss, garnet-biotite-muscovite schist (that may contain kyanite), and minor muscovite-bearing quartzite lenses. Scarce lenses of amphibolite are locally present. The upper units show partial melting features, locally, and are mainly composed of garnet-biotite-muscovite schist that commonly are kyanite-bearing, with intercalations of garnet-biotite($\pm$kyanite) paragneiss, high-pressure granulite (with rutile, kyanite, garnet and K-feldspar), and garnet amphibolite (Simões, 1995; Valeriano, Machado, et al., 2004). Based on this lithological succession, the metasedimentary pile of the Passos Nappe is interpreted as having evolved broadly from platform to pelagic settings. The metabasic rocks are classified as high- and low-TiO_2 tholeiites and have crystallization ages of ca. 0.9 Ga (Valeriano, Machado, et al., 2004; Valeriano & Simões, 1997). The predominance of the low-TiO_2 tholeiites towards the top of the Passos Nappe, along with the transition from psammitic to pelitic-dominated sedimentation, was interpreted by Valeriano and Simões (1997) as reflecting progressive thinning of the continental lithosphere during the evolution of the Neoproterozoic passive margin.

2.3 | Metamorphic record

Rocks from the Passos Nappe record an inverted metamorphic gradient (Luvizotto, 2003; Simões, 1995), ranging from greenschist-grade at the base (biotite-muscovite schist), to high-pressure granulite facies conditions at the top (kyanite-garnet gneiss with partial melting features). No precise P–T conditions are currently available for these rocks.

To the north of the Passos Nappe (Figure 1b), rocks from the Araxá group reached granulite facies in the Anápolis-Itauçu Complex (Pimentel, 2016; Piuzana et al., 2003a, 2003b), where ultra-high-temperature mineral assemblages are recognized (Baldwin et al., 2005; Moraes et al., 2002), but not at particularly high-pressure conditions ($\sim$0.9 GPa). High-pressure granulite facies metamorphism is only recognized in rocks from the top of the Andrelândia Nappe System, occurring further south than the Passos Nappe. Within the Andrelândia Nappe System, high-pressure granulites are recognized in the Três Pontas-Varginha and Pouso Alegre Nappes, and in the Carvalhos, Aiuruoca, and Serra da Natureza Klippen (Figure 1b). P-T conditions of these rocks have been calculated at 800–850°C and 1.2–1.4 GPa (Campos Neto et al., 1999, 2007, 2010; Cioffi et al., 2012; Coelho et al., 2017; da Motta & Moraes, 2017; Reno et al., 2009; Trouw, 1992) or for higher pressure conditions, between 1.5 and 1.8 GPa (Martinez, 2015).

2.4 | Ages

The age of peak metamorphism in the Passos Nappe, based on TIMS U-Pb zircon data from syn-tectonic leucosome veins, is 631 $\pm$ 4 Ma (Valeriano, Machado, et al., 2004). Monazite crystals collected from the leucosomes of migmatites, garnet biotite schists, and muscovite quartzite from the upper portion of the Passos Nappe indicate younger ages of ca. 605 Ma (Valeriano, Machado, et al., 2004). These monazite ages are interpreted to be associated with the exhumation and cooling of the nappe and are consistent, within uncertainties, with a rutile age of ca. 594 Ma (Valeriano, Machado, et al., 2004). Final cooling stages of the Passos Nappe are recorded by the youngest muscovite K-Ar ages near the studied area of ca. 570–580 Ma (Valeriano et al., 2000).

The high-pressure granulite from the Andrelândia Nappe System (Três Pontas-Varginha Nappe and Serra da Natureza Klippe, Carvalhos Klippe, Pouso Alegre Nappe and Aiuruoca Klippe, Figure 1b) is composed of rutile, kyanite, K-feldspar, garnet, and quartz, with a quartz-feldspathic leucosome (Campos Neto et al., 2010), very similar to the rocks studied here. A monazite age of 617.7 $\pm$ 1.3 Ma, obtained by Campos Neto et al. (2010), was interpreted as the age of the metamorphic peak of the Carvalhos Klippe. For the Serra da Natureza klippe, da Motta and Moraes (2017) obtained an age of matrix

monazite of 604.5 ± 6.1 Ma, which was also interpreted as dating the metamorphic peak. Reno et al. (2009, 2012) presented an older interval for the Três Pontas-Varginha Nappe rocks, indicating peak conditions at ca. 670–650 Ma (based on monazite from the matrix and inclusions in garnet). Younger ages of ca. 640–588 Ma, obtained from monazite crystals from the matrix, are interpreted by Reno et al. (2009, 2012) to be related to the retrograde path in the Três Pontas-Varginha Nappe, Carmo da Cachoeira Nappe, and Carvalhos Klippe.

Lenses of high-pressure metabasic rocks in the Andrelândia Nappe System contain inherited zircon grains with rims dated at ca. 630 and 605 Ma the first of which was interpreted as dating the pressure peak of eclogite facies metamorphism (Coelho et al., 2017; Frugis et al., 2018; Tedeschi et al., 2017).

3 | METHODS

A multi-approach method was applied to assess the *P-T*-t path of high-pressure granulites of the Passos Nappe. Thermodynamic modeling using constraints from mineral compositions and zoning were combined with Ti-in-quartz and Zr-in-rutile thermometry to constrain a detailed *P-T*-t path. In situ dating of monazite and rutile yields information about the timing of two stages within this metamorphic evolution.

3.1 | Optical and electron microscopy

Four representative samples (SSPDH10, SSPDH12, MG161, and SSPDH2; see location in Figure 1d) were prepared as standard polished thin sections and were studied with an optical polarizing microscope and using a JEOL JSM 6010LA scanning electron microscope (SEM) at the Department of Geology of São Paulo State University, Brazil (UNESP). The mineral proportions were estimated based on the optical polarizing microscope visual counts, field observations, and the proportions in the mineral distribution maps.

3.2 | Electron Probe Micro Analyzer

Quantitative analyses of mineral compositions, compositional maps, and trace element analyses of rutile and Ti-in-quartz were carried out using a JEOL JXA-8230 Electron Probe Micro Analyzer (EPMA) equipped with five wavelength dispersive spectrometry (WDS) detectors at the Department of Geology of UNESP.

WDS quantitative analyses of garnet, plagioclase, K-feldspar, and biotite were conducted using a of 5 μm diameter electron beam, with a 15 kV voltage and a 20 nA beam current. The counting times were set to 20 s for major element analysis and 30 s for minor element analysis, equally distributed on peak and background positions. Well-characterized natural and synthetic standards were used for calibration. Compositional mapping was carried out to (i) produce mineral distribution maps, (ii) to identify compositional variation within these minerals, and (iii) to calculate local bulk compositions used for the metamorphic modelling. Mapping was conducted at 15 kV and 100 nA, with step sizes ranging from 10 to 20 μm and dwell times from 60 to 200 ms, depending on the size of the map. The data were processed using the XMapTools 2.5.1 software (Lanari et al., 2014, 2019) to produce quantitative maps and extract local bulk compositions. Quantitative point analyses within the map area were used to calibrate X-ray maps.

Trace elements analyses in rutile followed the method outlined by Luvizotto et al. (2009) and were carried out under a focused beam, using an accelerating voltage of 20 kV and a current of 80 nA. Extended counting times were used to reduce relative uncertainties and to improve detection limits (Table 1). The following elements were analyzed: Si, Al, Cr, Fe, Ta, Nb, and Zr. Concentrations of Si were used as quality control to detect and avoid zircon inclusions and contamination from secondary

TABLE 1 Electron microprobe conditions used for the rutile trace elements analysis

20 kV/80 nA	Si	Al	Cr	Ta	Fe	Ti	Nb	Zr
Crystal	TAP	TAP	PETJ	LIFL	LIFL	PETJ	PETJ	PETJ
Line	Kα	Kα	Kα	Lα	Kα	Kβ	Lα	Lα
Peak sec[a]	300	300	150	150	150	30	300	300
Bkg sec[b]	150	150	50	50	50	15	150	150
DL[c]	25	20	50	85	40	55	40	45

[a]Count time on peak position in seconds.

[b]Count time on background position in seconds.

[c]2σ detection limit, based on repeated measurement of variation on background, values in μg/g.

fluorescence of neighboring silicates (all analyses with Si content above 300 μg/g were discarded). The R10 and Sy rutile reference materials (Luvizotto et al., 2009) were used as secondary standards to ensure the quality and reproducibility of analyses. Rutile thermometry calculations followed the calibration of Tomkins et al. (2007).

Analyses of Ti-in-quartz were performed using a 15 kV voltage and a beam current of 200 nA, using the Sy rutile (Luvizotto et al., 2009) as an analytical standard for Ti. Peak (400 s) and background (200 s) Ti measurements were carried out simultaneously on three WDS (PET crystals) spectrometers to improve counting statistics. With this setup, the minimum detection limit for Ti was 14 μg/g, considering background measurements and ZAF matrix correction factors. Ti-in-quartz temperatures were calculated following the calibration of Thomas et al. (2010).

Cathodoluminescence (CL) maps were produced to image the distribution of Ti-in-quartz and to investigate its textural relationships with other minerals. CL maps were acquired simultaneously with the compositional mapping, using a Hamamatsu H8259 CL system coupled to the JEOL JXA 8230 EPMA. An Astronomik L-RGB Type 2C blue filter (380 to 520 nm) was used for evaluating the Ti content in quartz (Kendrick & Indares, 2018a; Kidder et al., 2013; Leeman et al., 2012; Müller et al., 2002). The XMapTools 2.5.1 software (Lanari et al., 2014, 2019) was used to generate quantitative maps (Ti content in quartz based on the blue CL emission), with calibration using WDS quantitative point analyses within the map area.

EPMA monazite dating (U-Th-Pb$_T$) followed the recommendations of Williams et al. (2006). Full thin section X-ray mapping of Ce and P was done using a voltage of 15 kV, a beam current of 200 nA, dwell times of 20–50 ms, an electron beam size of 30 μm, and a step size of 30 μm. These maps were used to identify monazite crystals and examine their textural relationships with other phases. For selected monazite crystals, high-resolution compositional X-ray maps were collected for Y, Al, Th, U, Pb, Si, Ca, Fe, La, and Ce, with conditions of 15 kV, 100 nA, 100 ms dwell time, and 10 μm electron beam size and step. To compare concentration levels and zoning characteristics from crystal to crystal, X-ray maps collected for all crystals from the same sample were processed using the same color scale and same minimum and maximum intensity values. The maps were then used to target distinctive domains for spot analyses and age calculations. Unlike the procedure discussed by Williams et al. (2006), background measurements were performed for all analyses. Point analyses followed the method outlined by Vlach (2010), and the analytical conditions are presented in Table 2.

The specimen current varied from 80 to 100 nA and was constantly monitored to evaluate and avoid beam damage. Every 10 to 20 analyses were bracketed by three analyses of Moacir monazite secondary standard (Gonçalves et al., 2016). Spectral interference corrections were performed offline and considered matrix correction factors. Interference corrections and age calculations were performed using the Age_Cor program (Vlach, 2010). Uncertainties were calculated based on the relative standard error of each analysis, using the weighted average method in the Isoplot software (Ludwig, 2003). Systematic uncertainties were not propagated.

3.3 | LA-ICP-MS analyses

U-Pb rutile dating and trace element analyses in rutile and quartz used the Laser Ablation Inductively Coupled Plasma Mass Spectrometry (LA-ICP-MS) facilities at the Microgeochemistry Laboratory of the Department of Earth Sciences, University of Gothenburg, Sweden.

Rutile analyses were conducted using a New Wave NWR213 laser ablation system that was coupled to an Agilent 7500a quadrupole ICP-MS. Trace elements were analyzed with a 10 μm laser beam, surface energy of 4 J/cm^2, and a repetition rate of 10 Hz. The following isotopes were analyzed: ^{27}Al, ^{51}V, ^{53}Cr, ^{56}Fe, ^{90}Zr, ^{93}Nb, ^{95}Mo, ^{118}Sn, ^{121}Sb, ^{178}Hf, ^{181}Ta, ^{184}W, ^{208}Pb, ^{232}Th, and ^{238}U. For U-Pb rutile dating, analyses of trace elements in several crystals were initially performed, with high-U rutile crystals then selected for further analysis, following the recommendations of Zack et al. (2011). Isotopes were measured in time-resolved mode, with dwell times for each isotope for each mass scan of 10 ms for ^{90}Zr, ^{232}Th and ^{238}U, 30 ms for ^{206}Pb, and 50 ms for ^{207}Pb and ^{208}Pb. These analyses used a 50 μm diameter laser beam, at a laser energy of 5.6 J/cm^2 and a repetition rate of 10 Hz.

LA-ICP-MS analyses in quartz used a New Wave NWR213 laser ablation system coupled to an Agilent 8800 triple quadrupole. These analyses used a 10 μm diameter laser beam, with an energy of 6.7 J/cm^2 and repetition rate of 4 Hz. He was flushed through the ablation cup at the rate of 1 ml/min. The following isotopes were analyzed: ^{7}Li, ^{27}Al, ^{29}Si, ^{48}Ti, ^{49}Ti, ^{57}Fe, and ^{72}Ge. ^{49}Ti was used for calculations to avoid isobaric interference from ^{48}Ca, which is present in most well-characterized reference glasses containing ^{48}Ti.

In all LA-ICP-MS analyses, the signals were recorded over 60 s for each spot. The first 20 s were used to measure the background, the next 30 s for acquiring the analysis signal, and the last 10 s for system wash out. A He-Ar mixture was used as the carrier gas. The He was mixed with an Ar carrier and N, to enhance sensitivity.

TABLE 2 Electron microprobe conditions used for the monazite trace element analysis

Element	X-ray line	Crystal	CH	Acc. V	Peak Pos.	BG_L Pos.	BG_U Pos.	Peak (s)	BG (s)	High Volt.	Base Line	Window	Standard	Conc. Std. (%)	Curr. (A)	D.L. (ppm)
Y	La	TAP	1	15	70.048	1.25	1	100	50	1,635	3.5	3.2 (V)	Y2O3 P&H	11.80	1.00E-07	110
Si	Ka	TAP	2	15	77.314	1.65	1.05	40	20	1,630	2.2	4.1 (V)	Wollastonite P&H	50.96	2.00E-08	60
Al	Ka	TAP	2	15	90.577	2.47	1.72	40	20	1,630	2.2	4.1 (V)	Al2O3 P&H	99.99	2.00E-08	50
Th	Ma	PETJ	3	15	132.571	2	1.95	140	70	1,670	3.7	3.9 (V)	Th Glass MAC	5.90	1.00E-07	160
Ca	Ka	LIF	3	15	233.493	0.7	1.1	10	5	1,628	0.9	3.0 (V)	Apatita	54.02	2.00E-08	240
La	La	LIF	3	15	185.373	1.45	1.65	10	5	1,628	2.4	2.0 (V)	La2O3 P&H	11.50	2.00E-08	1,200
Ce	La	LIF	3	15	178.132	1.45	1.65	10	5	1,628	2.3	2.0 (V)	CeO2 P&H	11.90	2.00E-08	1,200
Pr	Lb	LIF	3	15	157.127	0.75	0.85	10	5	1,628	2.7	2.0 (V)	Pr6O11 P&H	12.20	2.00E-08	1,600
Nd	Lb	LIF	3	15	150.713	0.9	1	10	5	1,628	2.3	2.0 (V)	Nd2O3 P&H	11.80	2.00E-08	1900
Sm	Lb	LIF	3	15	139.059	0.55	0.55	10	5	1,628	3.2	1.8 (V)	Sm2O3 P&H	11.20	2.00E-08	1800
Fe	Ka	LIF	3	15	134.693	0.75	0.65	10	5	1,628	2.4	3.1 (V)	Ilmenite PMCS	35.03	2.00E-08	400
Gd	Lb	LIF	3	15	128.512	1	1	10	5	1,628	3.5	2.1 (V)	Gd2O3 P&H	12.10	2.00E-08	1800
Er	La	LIF	3	15	124.195	0.75	0	10	5	1,628	3.3	2.3 (V)	Er2O3 P&H	11.90	2.00E-08	1,130
Tb	Lb	LIF	3	15	123.669	0.45	0	10	5	1,628	3.7	2.0 (V)	Tb4O7 P&H	11.90	2.00E-08	2,200
Dy	Lb	LIF	3	15	119.035	0.65	0.55	10	5	1,628	3.7	2.3 (V)	Dy2O3 P&H	12.00	2.00E-08	1960
Yb	La	LIF	3	15	116.35	1.5	1.45	10	5	1,628	3	2.0 (V)	Yb2O3 P&H	12.00	2.00E-08	1,430
U	Mb	PETL	4	15	118.932	3.98	3.98	300	150	1,670	3	2.7 (V)	UO2 MAC	99.80	1.00E-07	65
S	Ka	PETL	4	15	172.02	-	2	10	5	1,670	3	2.5 (V)	PbS P&H	33.46	2.00E-07	160
P	Ka	PETH	5	15	197.105	2.1	2.65	10	5	1,686	1.7	3.0 (V)	Apatita	40.78	2.00E-08	150
Pb	Ma	PETH	5	15	169.251	3.65	4.2	300	150	1,686	1.8	3.0 (V)	PbS P&H	93.29	2.00E-07	40

Abbreviations: Acc. V, acceleration voltage; BG (s), counting time on each background (upper and lower) position in s; BG_L Pos., lower background position in s; BG_U Pos., upper background position in mm from the peak; BG_U Pos., upper background position in mm from the peakCH, Spectrometer Chanel; Conc. Stds (%), concentration of the element in the standard; Curr. A, current of standard analyses in A; D.L., minimum detection limit (3 sigma) for the unknowns; Peak Pos., peak position in mm; Peak (s), counting time on peak position in s.

Each block of 10 unknown measurements was separated by two to three analyses of reference materials, using the R10 standard for rutile (Luvizotto et al., 2009) and the NIST SRM 610 and the Audetat quartz (Audétat et al., 2015) for quartz.

3.4 | Whole rock X-ray fluorescence

Bulk-rock compositions were obtained by X-ray fluorescence (XRF) at the Department of Geology of UNESP. Representative sample powders were mixed with lithium tetraborate to obtain fused disks that were analyzed with a Philips PW 2400. Loss on ignition (LOI) was determined by the conventional gravimetric method. XRF results were used for bulk-rock compositions comparison between the samples.

3.5 | Phase equilibria modelling

Phase diagrams were calculated in the $Na_2O–CaO–K_2O–FeO–MgO–Al_2O_3–SiO_2–H_2O–TiO_2–O_2$ (NCKFMASHTO) chemical system using version 3.40 of THERMOCALC (Powell et al., 1998; Powell & Holland, 1988), the ds6.2 internally consistent data set of Holland and Powell (2011), updated in February 2012, and the activity-composition models of White et al. (2014). The whole-rock compositions used in the phase equilibria modeling were based on the quantitative maps. A low extra oxygen content of 0.01 mol% O_2 was used in all pseudosections, since studied samples are ilmenite- and rutile-bearing and hematite-free. Contours of mineral compositions and isomodes were generated using TCInvestigator 1.0 (Pearce et al., 2015).

4 | RESULTS

4.1 | Petrography

The investigated unit is a para-derived rutile-kyanite-garnet-K-feldspar granulite with a stromatic structure in which banding is parallel to the main foliation (Figure 2). The rock is coarse-grained, and the studied samples (SSPDH10, SSPDH12, MG161, and SSPDH2) show only slight differences in modal proportions and in textural and structural characteristics (Figure 2).

Samples SSPDH10, SSPDH12, and MG161 contain porphyroblasts of garnet (up to 12 mm; ~30 vol%) and kyanite (up to 10 mm, ~5 vol%) (Figure 2a–f). The melanosome and leucosomes contain quartz (~35 vol%),

K-feldspar (~20 vol%), and plagioclase (less than 5 vol%), the distribution of these phases defining a foliation. Biotite only occurs in the melanosome (trace to less than 5 vol%). Minor phases include apatite, rutile, zircon, ilmenite, and monazite. Sample SSPDH2 also contains large, elongate garnet (up to 30 mm, ~15 vol%) and kyanite (up to 50 mm, ~20 vol%) porphyroblasts. Its melanosome and leucosomes consist of quartz (~30 vol%) and K-feldspar (~30 vol%). Biotite (± 5%) occurs in the matrix. Rutile, ilmenite, monazite, and zircon are minor phases. Plagioclase is absent in sample SSPDH2, which also has a better defined foliation than the other samples. The peak mineral assemblage of all samples is interpreted to be quartz + garnet + kyanite + K-feldspar + rutile + melt ± plagioclase.

4.1.1 | Garnet

In samples SSPDH10, SSPDH12, and MG161, garnet is sub-rounded (Figure 2a–d), poikiloblastic, and usually shows resorbed rims. The abundance of inclusions varies from sample to sample. In samples SSPDH10, MG161, and SSPDH12, inclusions of rutile, quartz, plagioclase, apatite, monazite, kyanite, and zircon are predominantly in garnet cores and inner rims (Figure 2a,e). Fewer inclusions of the same minerals occur in outer rims, where polymineralic inclusions of plagioclase, quartz, and K-feldspar are also present (Figure 2f–i). Garnet crystals in sample SSPDH2 are usually elongated and contain inclusions of lobate quartz (Figure 2d), K-feldspar, rutile, and kyanite. In all samples, garnet is in sharp contact with the kyanite porphyroblasts. The presence of inclusions in garnet of rutile, quartz, K-feldspar (only in garnet rims), kyanite, and apatite suggests their coexistence along the prograde path, prior to and/or during garnet growth.

4.1.2 | Kyanite

Kyanite occurs mainly in the melanosome and rarely as small inclusions in garnet. In all samples, based on textural evidence, it is possible to distinguish two types of kyanite. The first type consists of deformed crystals (undulose extinction) with small, rare inclusions of quartz, plagioclase, monazite, and rutile (Figure 3a,c,d). The second type of kyanite lacks undulose extinction and contains more and larger inclusions (Figure 3b–d). These inclusions of rutile, quartz, plagioclase, K-feldspar, monazite, zircon, and apatite are rounded in samples SSPDH10, SSPDH12, and MG161 and lobate in sample SSPDH2. Apatite only occurs as inclusion in the second

FIGURE 2 Images of the studied samples. (a) Photograph of sample SSPDH10. (b) Garnet porphyroblast with quartz and rutile inclusions. Garnet is zoned and inclusions are concentrated in the core and inner rim. Garnet is surrounded by biotite (sample SSPDH10, plane-polarized light). (c) Elongated garnet porphyroblast with quartz, rutile, and K-feldspar inclusions (sample SSPDH2, plane-polarized light). (d) Garnet porphyroblast with rutile and quartz inclusions and biotite in the garnet rim (sample MG161, plane-polarized light). (e) Garnet porphyroblast with zoned quartz and rutile inclusions, surrounded by biotite (sample SSPDH12, plane-polarized light). (f) Polymineralic inclusion in garnet, composed of plagioclase, quartz, monazite, and biotite (sample SSPDH10, back-scattered electron image). (g) Polymineralic inclusion in garnet, composed of quartz and K-feldspar (sample SSPDH10, back-scattered electron image). (h) Polymineralic inclusion in garnet, composed of plagioclase, quartz, apatite and K-feldspar (sample MG161, back-scattered electron image). (i) Polymineralic inclusion in garnet, composed of quartz and plagioclase (sample SSPDH12, back-scattered electron image). Mineral abbreviations after Kretz (1983) [Colour figure can be viewed at wileyonlinelibrary.com]
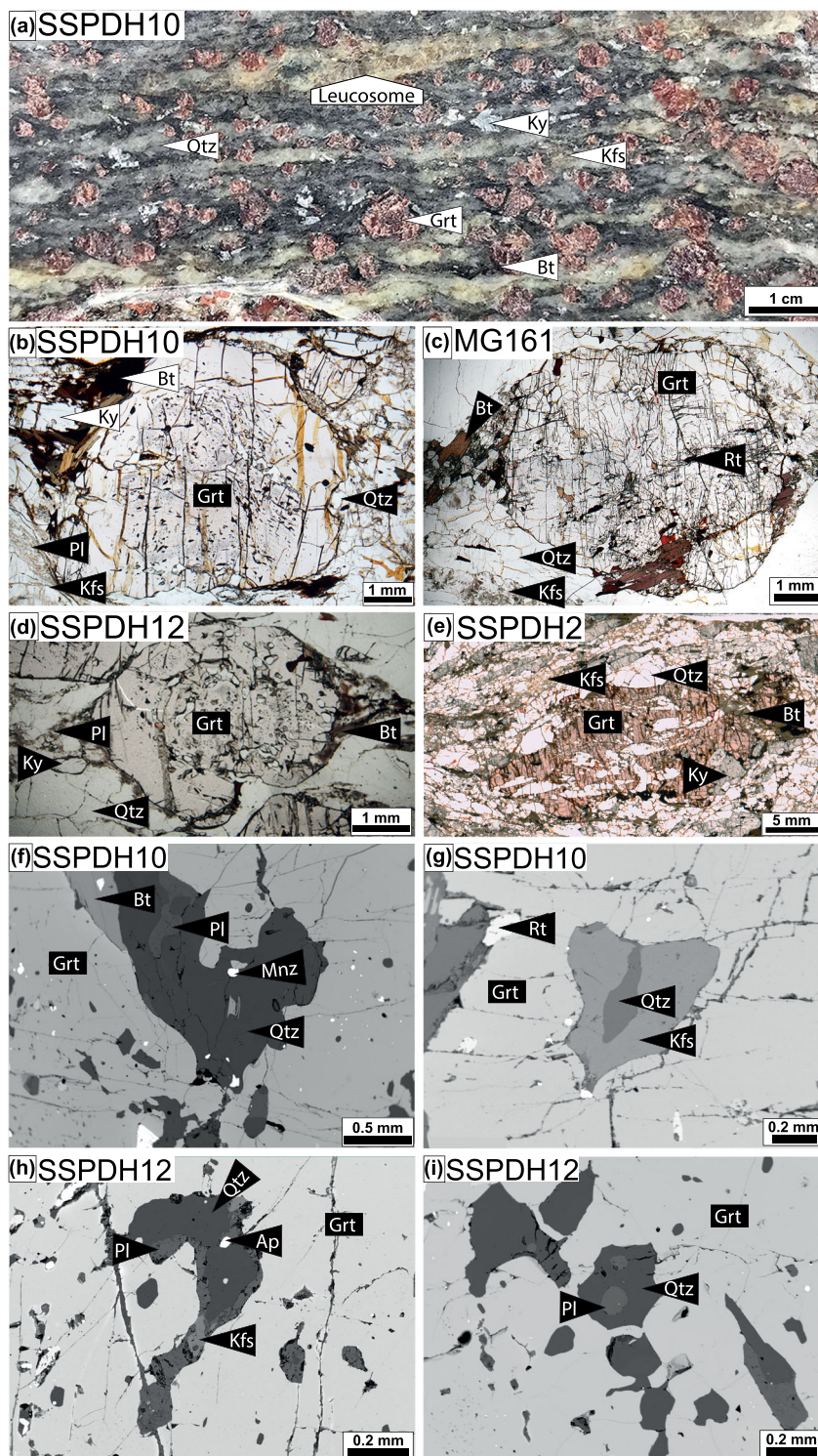
type of kyanite. Based on these textural variations, it is interpreted that the more deformed type of kyanite crystallized earlier, at the prograde metamorphism in sample SSPDH2 and in the peak metamorphism in the sample SSPDH10, while the second type of kyanite is interpreted to have crystallized later, during retrograde metamorphism in both samples.

4.1.3 | Host gneiss

In all samples, the quartz, K-feldspar and plagioclase (the latter absent in sample SSPDH2) in the melanosome are highly strained. These minerals present a bimodal size distribution, with aggregates of small, recrystallized grains of approximately uniform size ($<500\,\mu m$) filling
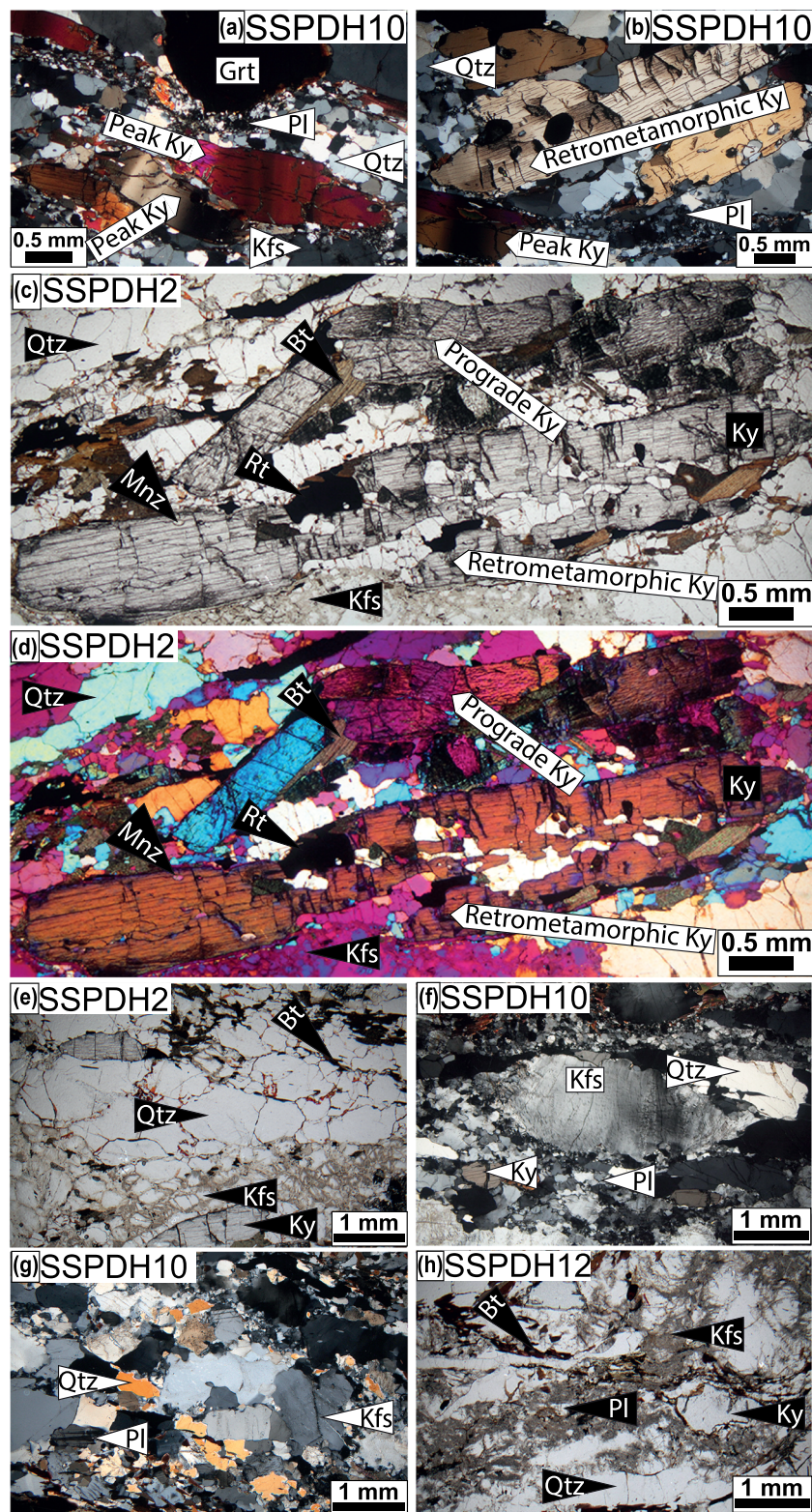
FIGURE 3 Photomicrographs of the studied samples. (a) Kyanite crystals with undulose extinction (sample SSPDH10, crossed-polarized light). (b) Kyanite crystals with quartz and rutile inclusions (sample SSPDH10, crossed-polarized light). (c and d) Kyanite crystals with undulose extinction (top of the image) and kyanite crystal with quartz, rutile and biotite inclusions (bottom of the image) (sample SSPDH2, plane-polarized light in c and crossed-polarized light with accessory gypsum plate in d). (e) Melanosome composed of quartz and K-feldspar (sample SSPDH2, plane-polarized light). (f) Melanosome composed of a large K-feldspar crystal and recrystallized quartz and plagioclase (sample SSPDH10, crossed-polarized light). (g) Melanosome composed of K-feldspar, quartz, and plagioclase (sample SSPDH10, crossed-polarized light). Quartz with K-feldspar and plagioclase is interpreted to have crystallized from a melt. (h) Melanosome composed of quartz, plagioclase, K-feldspar, and biotite (sample SSPDH12, plane-polarized light). Abbreviations after Kretz (1983) [Colour figure can be viewed at wileyonlinelibrary.com]

the spaces between larger grains that reach several millimeters (Figure 3e–h). Quartz, K-feldspar, and plagioclase display undulose extinction. Textural features of quartz and plagioclase indicate dynamic recrystallization by grain boundary migration and subgrain rotation (Figure 3). K-feldspar is coarser grained than plagioclase.

As the rocks are highly strained, textures recording crystallization of any trapped anatectic melt in the matrix are not preserved. However, the lobate polymineralic inclusions (Figure 2f–i) of quartz, plagioclase, and K-feldspar in garnet are interpreted as former melt inclusions and are locally found filling fractures in garnet (Figure 2h). It

is interpreted that most of the K-feldspar, particularly the large crystals in the melanosome, the plagioclase and the garnet (Figure 3f,h) crystallized near the metamorphic peak, with minor additional growth of plagioclase and K-feldspar during melt crystallization on the retrograde path.

4.1.4 | Leucosome

In the field, millimeter size layers of quartz and feldspar, which occur parallel to the rock foliation, serve as clear evidence of melt (Figure 2a). However, textures related to leucosome crystallization were obliterated by later deformation and dynamic recrystallization and are not preserved in thin section scale. The leucosome ($\sim$10 vol%, based on field observation) is composed of quartz, K-feldspar and plagioclase. These are finer grained than those in the matrix outside the leucosome. Clusters of quartz, plagioclase, and K-feldspar, interpreted as leucosome, also occur bordering the garnet and kyanite porphyroblasts. Quartz commonly occurs in K-feldspar and plagioclase aggregates, again indicative of its formation during melt crystallization. The garnet lobate polymineralic inclusions (Figure 2f–i) described above are interpreted as leucosome-forming melts trapped within the garnet.

4.1.5 | Biotite and minor phases

Biotite crystals are anhedral and occur bordering garnet, mostly in strain shadows, and kyanite. Biotite also fills fractures in these minerals (Figure 2b–e) and is interpreted to be a retrograde phase. Rutile occurs in the melanosome or leucosome domain and as inclusions in garnet and kyanite in all studied samples. Ilmenite replaces and occurs as fine lamellae in rutile. Zircon crystals are euhedral to subhedral and occur in the mineral matrix, in the leucosome, and as inclusions in garnet and kyanite crystals. In all samples, monazite is found in the melanosome and leucosome, and as inclusions in garnet and more rarely kyanite. Apatite occurs as small crystals in the melanosome, in the leucosome, and as inclusions in garnet rims in samples SSPDH10, SSPDH12, and MG161.

4.2 | Mineral Chemistry

4.2.1 | Garnet

Garnet crystals display a complex chemical zoning (Figures 4b–e,j–m and S1 and Table S1). The main grain

pictured in Figure 4b–e, from sample SSPDH10, has a roughly centered core region. A rounded core, with higher spessartine content (X_{Sps} core: 0.02–0.025, rim: 0.01–0.02) contrasts in shape with the core regions observed for almandine, pyrope, and grossular (Figure 4b–e). Overall, the core has higher grossular content (X_{Grs} core: 0.11–0.16, rim: 0.05–0.10), while mantles and rims have higher almandine (X_{Alm} core: 0.57–0.59, rim: 0.595–0.63) and pyrope contents (X_{Prp} core: 0.22–0.28, rim: 0.28–0.34). Locally, an outer rim with the highest almandine proportion (0.63), intermediate pyrope (0.26), and higher spessartine proportion (0.025) is observed (Figure 4b–e). The high grossular inner core is rutile-free. Garnet X_{Fe} ranges from 0.67 in the core to 0.64 in the rim.

Garnet crystals in samples SSPDH12 (Figure S1) and MG161 (Table S1) have similar compositional and zoning patterns to those in SSPDH10, but with spatially off-centered compositional core regions. These cores have relatively high grossular content (0.04–0.09) and low almandine (0.64–0.70) and pyrope contents (0.27–0.35) (Figure S1 and Table S1). Locally, an outer rim has higher spessartine and pyrope contents and lower almandine content. The spessartine content varies from 0.01 to 0.02. The X_{Fe} ranges from 0.63 (rim) to 0.70 (core).

Garnet compositions in sample SSPDH2 are substantially different from the other studied samples, but the general zoning patterns are similar. This sample is more strained, with distinctly elongated garnet grains. A sub-rounded, off-centered core with lower almandine and higher pyrope and grossular contents is observed. This core region is not apparent in the spessartine map. An outer rim with higher almandine, grossular, and spessartine contents and lower pyrope content occurs locally. The almandine content ranges from 0.70 (core) to 0.71 (rim/mantle) and 0.77 (outer rim), coexisting with pyrope contents of 0.21 (core), 0.23 (rim/mantle), and 0.18 (outer rim) and grossular contents of 0.065 (core), 0.033 (rim/mantle), and 0.05 (outer rim). The spessartine content ranges from 0.13 (core/mantle/rim) to 0.022 (outer rim). In sample SSPDH2, the X_{Fe} ranges from 0.83 in the core to 0.93 in the rim.

4.2.2 | Plagioclase

In all plagioclase bearing samples (SSPDH10, SSPDH12, and MG161), plagioclase is sodic (Figure 4f and Table S1), with X_{an} of 0.23–0.33 with no systematic zoning is observed. Plagioclase adjacent to garnet has the same composition as grains from the leucosome layer (Figure 4f).
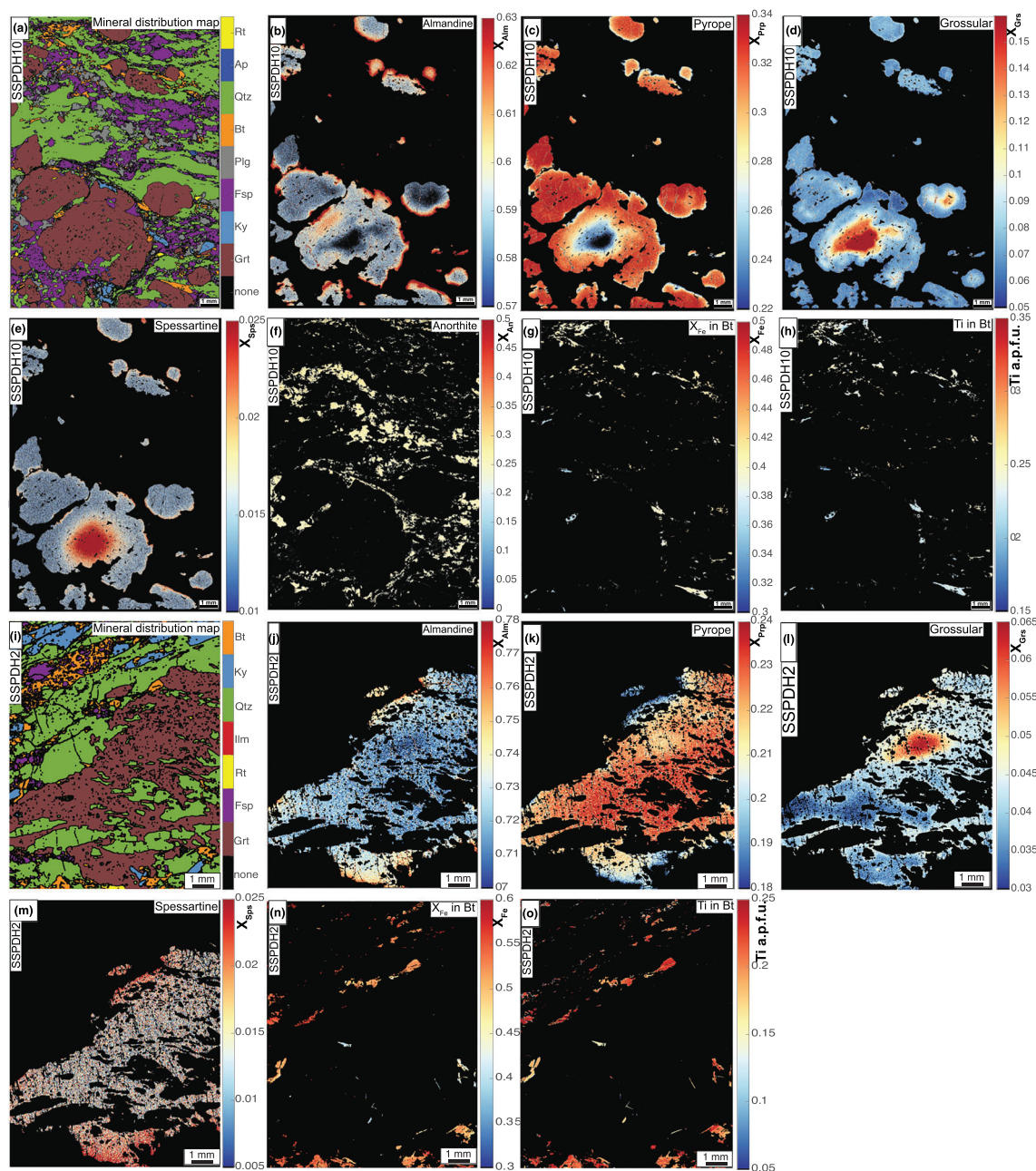
FIGURE 4 Mineral compositional maps for samples SSPDH10 and SSPDH2. (a) Mineral distribution map from sample SSPDH10. (b–e) Almandine, pyrope, grossular, and spessartine zoning in garnet, respectively (where $X_{Alm} = Fe/[Fe + Ca + Mg + Mn]$, $X_{Py} = Mg/[Fe + Ca + Mg + Mn]$, $X_{Grs} = Ca/[Fe + Ca + Mg + Mn]$, and $X_{sps} = Mn/[Fe + Ca + Mg + Mn]$) for sample SSPDH10. (f) Anorthite content of plagioclase for sample SSPDH2. (g) Proportion of X_{Fe} in biotite ($X_{Fe} = Fe/[Fe + Mg]$) from sample SSPDH10. (h) Ti content in biotite from sample SSPDH10. (i) Mineral distribution map for sample SSPDH2. (j–m) Almandine, pyrope, grossular, and spessartine zoning in garnet, respectively (where $X_{Alm} = Fe/[Fe + Ca + Mg + Mn]$, $X_{Py} = Mg/[Fe + Ca + Mg + Mn]$, $X_{Grs} = Ca/[Fe + Ca + Mg + Mn]$, and $X_{sps} = Mn/[Fe + Ca + Mg + Mn]$) from sample SSPDH2. n) Proportion of X_{Fe} in biotite ($X_{Fe} = Fe/[Fe + Mg]$) for sample SSPDH2. (o) Ti content in biotite for Sample SSPDH2 [Colour figure can be viewed at wileyonlinelibrary.com]

4.2.3 | Biotite

In all samples, X_{Fe} and Ti in biotite increase with distance from garnet (Figure 4g,h and Table S1), as observed in previous studies (Lasalle & Indares, 2014; Spear & Parrish, 1996). The Ti content ranges from 0.19 atoms per formula unit (a.p.f.u.) to 0.26 a.p.f.u. and the X_{Fe} from 0.37 to 0.58 in samples SSPDH10, SSPDH12, and MG161. In sample SSPDH2, the Ti content in biotite ranges from 0.15 to 0.25 a.p.f.u. and the X_{Fe} from 0.40 to 0.56 (Figure 4n,o).

4.3 | Rutile thermometry

Rutile occurs in all studied samples, in the matrix and as inclusions in garnet and kyanite (Figure 5). We present the full rutile trace element dataset in Table S2, Zr concentrations in Figure 6, and descriptive statistics of Zr contents in rutile in Table 3.

Sample SSPDH12 contains rutile included in garnet (Figure 5a) and in the matrix. These rutile crystals are subhedral, with an average size of 120 μm, reaching up to 250 μm. Some rutile crystals contain ilmenite lamellae and rare rounded zircon inclusions. Zr contents in grains included in garnet vary between 912 and 1,795 μg/g, with variation of 1,511–1,737 μg/g in grains in the matrix. Concentrations of Zr-in-rutile above the 90th percentile range from 1,793 to 1,795 μg/g, corresponding to a calculated temperature of 830°C (at 1.2 GPa).

Rutile crystals in sample MG161 are subhedral and occur either in the matrix or included in garnet and kyanite, averaging 200 μm in length and reaching up to 800 μm (Figure 5b,c). Ilmenite lamellae and zircon inclusions are present in almost half of the crystals. In rutile crystals included in garnet, Zr contents vary from 767 to 1,742 μg/g. Those from the matrix contain 856 to
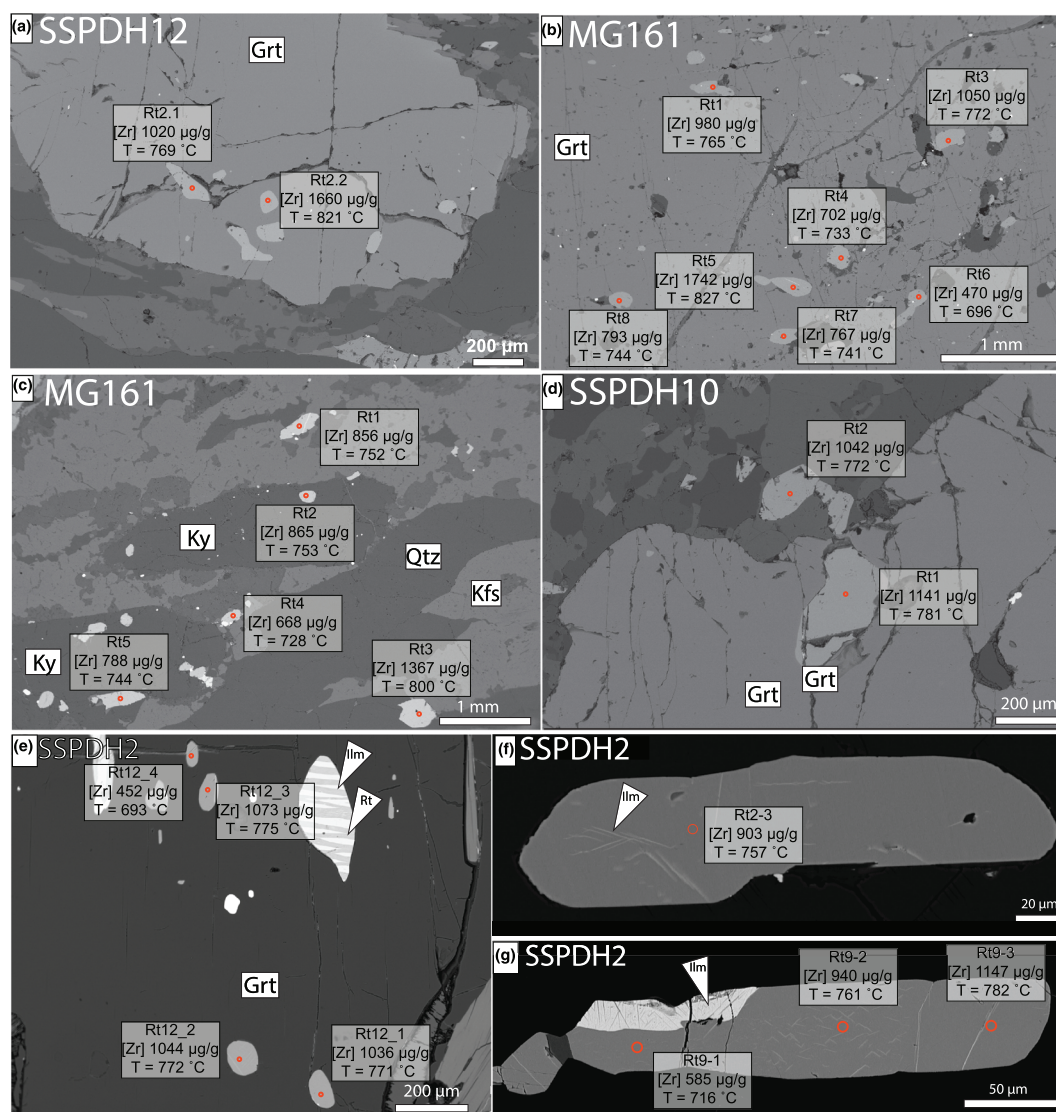

FIGURE 5 Back-scatter electron images of analyzed rutile crystals. Temperature calculations at 1.2 GPa. (a) Rutile crystals Rt2.1 and Rt2.2 included in garnet from sample SSPDH12. (b) Some of the analyzed rutile grains from sample MG161 included in the garnet. (c) Some of the analyzed crystals from sample MG161. Rt2 and Rt5 are included in kyanite, and Rt1, Rt4, and Rt3 are in the matrix. (d) Two rutile crystals (Rt1 and Rt2) analyzed from sample SSPDH10, R1 is included in the rim of garnet, and Rt2 is in the matrix. (e) Analyzed rutile crystals included in garnet from sample SSPDH2. (f) Rutiles 2–3 included in kyanite and containing ilmenite lamellae, from sample SSPDH2. (g) Rutile 9 included in garnet from sample SSPDH2. Note ilmenite in part of the rutile rim and faint ilmenite lamellae throughout [Colour figure can be viewed at wileyonlinelibrary.com]
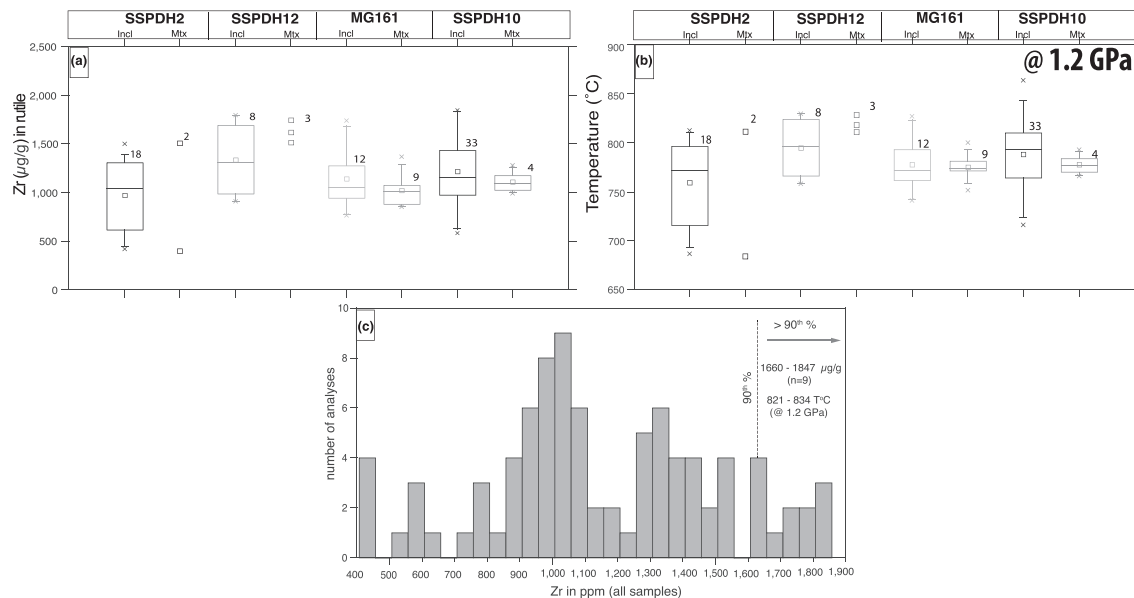
FIGURE 6 Box and whisker plots showing concentration (in µg/g) of Zr-in-rutile crystals (a), resultant Zr-in-rutile temperatures (at 1.2 Gpa) (b). Data from rutile included in garnet and kyanite crystals (Incl) are separated from matrix rutile (Mtx). Whiskers represent the 10th and 90th percentile, and boxes represent the second (bottom, 25%) and third quartile (top, 75%). For rutile grains with more than one spot, only one representative analysis is plotted. The minimum and maximum values are plotted as "x," the small squares represent the median value, and the lines represent the mean value. The numbers at the top-right of each box represent the number of analyses for that sample. For samples in which less than three analyses are above detection limits, the values of each analysis are plotted as small squares. (d) Combined histogram of the Zr content of rutile in all analyses

TABLE 3 Summary of Zr-in-rutile content in analyzed samples. Temperature calculated at 1.2 GPa. Min.: minimum, Max: maximum, Stdev 2 s.: Standard derivation using 2 sigma, Incl: rutile crystals included in garnet or kyanite, Mtx: rutile crystals that occur in the matrix

		Number	Min	Max	1st Quartile	Median	3rd Quartile	Mean	Stdev 2 s
SSPDH2C Incl	Zr (µg/g)	18	422	1,503	620	1,040	1,308	975	723
	T (°C) @1.2 GPa	18	687	813	715	772	815	759	42
SSPDH2 Mtx	Zr (µg/g)	2	407	1,510	683	959	1,234	959	1,560
	T (°C) @1.2 GPa	2	684	811	690	747	816	747	89
SSPDH12 Incl	Zr (µg/g)	8	912	1,795	994	1,316	1,692	1,340	748
	T (°C) @1.2 GPa	8	758	830	765	796	825	795	30
SSPDH12 Mtx	Zr (µg/g)	3	1,511	1,737	1,561	1,612	1,674	1,620	227
	T (°C) @1.2 GPa	3	811	827	815	818	824	818	8
MG161 Incl	Zr (µg/g)	12	767	1,742	951	1,046	1,278	1,141	626
	T (°C) @1.2 GPa	12	741	827	760	772	825	778	27
MG161 Mtx	Zr (µg/g)	9	856	1,367	886	1,010	1,075	1,027	333
	T (°C) @1.2 GPa	9	752	800	772	774	800	775	12
SSPDH10 Incl	Zr (µg/g)	30	585	1,847	977	1,096	1,422	1,171	648
	T (°C) @1.2 GPa	30	716	863	762	793	865	788	36
SSPDH10 Mtx	Zr (µg/g)	4	990	1,282	1,029	1,091	1,176	1,114	257
	T (°C) @1.2 GPa	4	166	793	772	776	790	778	11

1,367 µg/g Zr. Values above the 90th percentile range from 1,587 to 1,742 µg/g, indicating temperatures of 816 to 827°C (at 1.2 GPa).

Sample SSPDH10 contains large rutile crystals as inclusions in garnet and in the matrix (Figure 5d). Rutile crystals are subhedral with an average of 200 µm in

length, occasionally reaching 500 µm. In this sample, tiny ilmenite lamellae occur in some crystals, and zircon inclusions in rutile are rare. Zr contents in rutile range from 585 to 1,847 µg/g in grains included in garnet and from 990 to 1,282 µg/g in those from the matrix (four LA-ICP-MS analyses). Zr contents above the 90th percentile range from 1,673 to 1,847 µg/g, yielding temperatures of 822°C to 837°C (at 1.2 GPa).

Rutile crystals in sample SSPDH2 occur as inclusions in garnet and kyanite (Figure 5e–g) as well as in the matrix. The average size of rutile is around 200 µm, reaching up to 500 µm. The crystals are mainly anhedral, but some subhedral crystals are also present. Virtually all rutile crystals in sample SSPDH2 have ilmenite lamellae (Figure 5e–g), but zircon inclusions are rare. Zirconium contents in these rutile crystals show the largest variation of all analyzed samples: rutile in inclusions contains 423–1,503 µg/g Zr and those in the matrix grains contain 408–1,510 µg/g. Values above the 90th percentile range from 1,489 to 1,510 µg/g, corresponding to temperatures of 809°C to 811°C (at 1.2 GPa).

A summary of the Zr content of all analyzed rutile grains is presented in Figure 6c. In total, nine values are above the 90th percentile, and the maximum Zr content is 1,847 (sample SSPDH10). Considering only these

values, the calculated temperatures range from 821°C to 834°C (at 1.2 GPa).

4.4 | Quartz thermometry

The full dataset of Ti-in-quartz analyses is presented in Table S3. A summary, with descriptive statistics, is presented in Table 4. In samples SSPDH2 and SSPDH10, the Ti content of quartz ranges from 26 to 134 µg/g ($n = 178$ analyses and quantitative map) and 25 to 130 µg/g ($n = 179$ analyses and quantitative map), respectively (Figures 7–9). CL maps of these two samples show that the highest Ti values tend to occur in the core (i.e., central region of large grains) and decrease towards the rims (Figures 8b,g and 9b), for both matrix grains that are included in garnet. In some quartz agglomerates, the high Ti domains in the quartz are rather patchy (Figure 9h). In samples MG161 and SSPDH12, Ti contents in quartz vary from 27 to 95 µg/g ($n = 14$) and from 23 to 99 µg/g ($n = 21$), respectively (Figure 7).

As a novel approach to further evaluate the Ti distribution, CL maps were converted into Ti content maps by referencing spot analyses in XMapTools and using the advanced calibration method

TABLE 4 Summary of Ti-in-quartz content in analyzed samples. Min.: minimum, Max: maximum, Stdev 2 s.: Standard derivation using 2 sigma. T.: temperature in °C

|	SSPDH2			SSPDH10		
	Ti (µg/g)	T @0.7 GPa	T @1.2 GPa	Ti (µg/g)	T @0.7 GPa	T @1.2 GPa
Number	178	178	178	179	179	179
Min	26	564	663	25	559	658
Max	134	719	837	119	705	822
1 st Quartile	44	610	710	66	635	755
Median	58	631	739	82	666	777
3rd Quartile	74	653	760	95	670	795
Mean	62	633	741	79	659	770
Stdev 2 s	48	35	39	37	26	29
	MG161			SSPDH12		
	Ti (µg/g)	T @0.7 GPa	T @1.2 GPa	Ti (µg/g)	T @0.7 GPa	T @1.2 GPa
Number	14	14	14	21	21	21
Min	27	567	667	23	555	654
Max	95	681	795	99	685	800
1 st Quartile	53	628	725	58	630	740
Median	67	646	755	62	640	748
3rd Quartile	69	655	762	84	670	773
Mean	60	633	740	68	644	754
Stdev 2 s	36	31	35	39	31	35
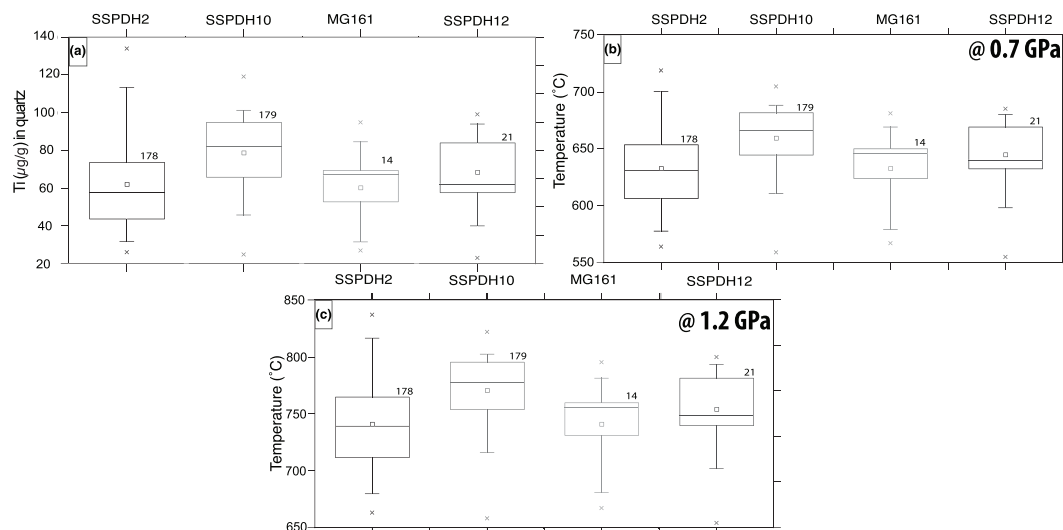
FIGURE 7 Box and whisker plots showing concentration (in μg/g) of Ti-in-quartz (a) and the resultant Ti-in-quartz temperatures assuming 0.7 GPa (b) and 1.2 GPa (c). Whiskers represent the 10th and 90th percentile. Boxes represent the second (bottom, 25%) and third quartile (top, 75%). The minimum and maximum values are plotted as "x," the small squares represent the median value, and the lines represent the mean value. For rutile grains with more than one spot, only one representative analysis is plotted. The numbers at the top-right of each box represent the number of analyses for that sample

(Lanari et al., 2019). Figures 8 and 9 emphasize that the Ti content of quartz in the studied samples is extremely heterogeneous, with concentrations decreasing from core to rim. Few patches of Ti content higher than 115 μg/g are preserved.

Considering pressure conditions of 1.2 GPa, the calculated temperatures results range from ~654°C to 837°C, while for 0.7 GPa, the results would range from ~555°C to 719°C (Figures 8 and 9 and Table 4).

4.5 | Phase equilibria

Studied samples SSPDH10, SSPDH12, and MG161 have similar modal proportions of minerals, mineral compositions, and bulk rock compositions (Table S4). Thus, the pseudosections calculated for sample SSPDH10 (Figure 10a,b) are assumed to be representative of these studied samples. Since sample SSPDH2 is plagioclase free and has slightly different bulk rock composition (Table S4), a separate set of pseudosections was calculated for it (Figure 10). Two sets of phase equilibria were calculated. First, a pseudosection using the local bulk rock composition from the maps, but removing material from the garnet core was calculated (Figure 10a,c). Here, the bulk rock H_2O content was set to 1.00 mol% for sample SSPDH10 and 0.81 mol% for sample SSPDH2, which corresponds to the amount of water stored in the hydrous phases (biotite) observed in each sample. These pseudosections were used to infer the peak and retrograde

conditions. Second, a set of pseudosections was calculated to estimate the prograde conditions, in which melt and the garnet core composition was re-integrated into the bulk rock composition used to calculate the previous set (Figure 10b,d). Sufficient melt was re-integrated to bring the solidus down-T to H_2O saturated conditions (Indares et al., 2008; Lasalle & Indares, 2014; White et al., 2004). This corresponded to 16% reintegrated melt for sample SSPDH10 and 15% for SSPDH2 (Figure 10b,d). Garnet, quartz, K-feldspar, biotite, muscovite, rutile, kyanite, sillimanite, and silicate melt are all stable in regions of the investigated P-T window and in all pseudosections. Plagioclase only occurs in the pseudosections for sample SSPDH10.

The inferred peak mineral assemblage of garnet + kyanite + K-feldspar + rutile + melt + quartz + plagioclase is predicted to be stable, in the "peak-PT conditions" pseudosection calculated for sample SSPDH10 at T higher than 800°C and P between 1.1 and 1.7 GPa (Figure 10a). Retrograde biotite is observed in the rock, with biotite stability only calculated at T lower than 820°C (Figure 10a) in the kyanite stability field (sillimanite is absent in the rock and kyanite appears to have been the stable Al_2SiO_5 polymorph throughout). Ilmenite is only predicted to be stable at pressure below 0.52 GPa and temperatures below 575°C, considering the kyanite stability (Figure 10a).

According to the peak condition pseudosection calculated for sample SSPDH2 (Figure 10c), the peak mineral assemblage of garnet + kyanite +

K-feldspar + rutile + melt + quartz is stable above 790°C and above 0.98 GPa. Retrograde biotite is also observed in this sample and occurs below 790°C and 1.11 GPa (Figure 10c). Ilmenite is calculated to be stable below 705°C and 0.8 GPa (Figure 10c), considering the kyanite stability fields.

Dehydration melting of muscovite occurs in the melt generation, as it is common in most pelites (Figure 10a,c), according to the generalized reaction:

$$Ms \pm Pl + Qtz = Ky + Ksp + Liq.$$
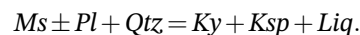
In sample SSPDH2, kyanite occurs in all fields in the pseudosections. On the other hand, in sample SSPDH10, kyanite is absent throughout the prograde fields (Figure 10b) and is present in the peak assemblage field (Figure 10a), according to the muscovite-out reaction above.
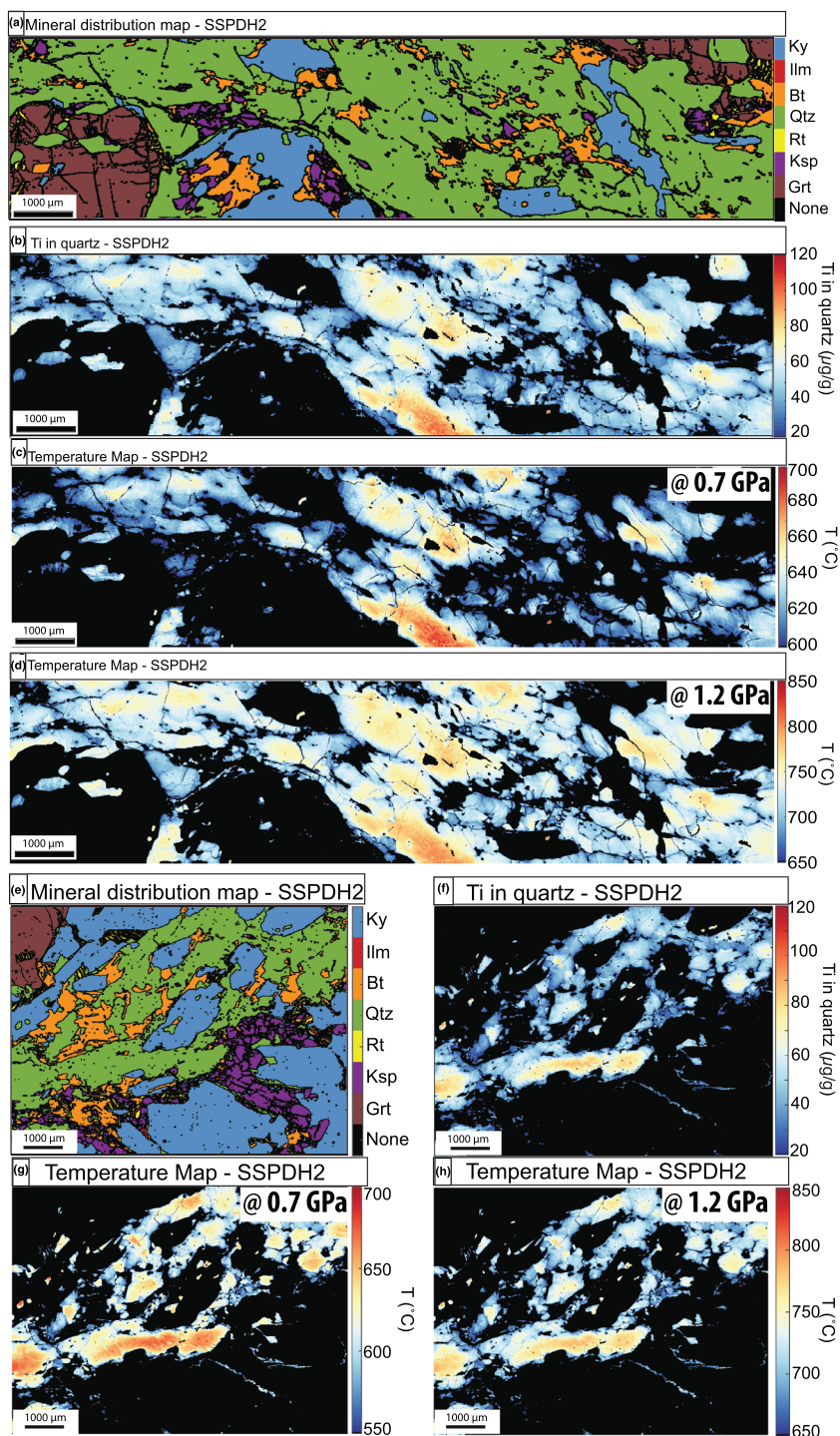

FIGURE 8 Quartz textures and compositions in sample SSPDH2. (a) Mineral distribution map showing the occurrence of matrix quartz and quartz inclusions in garnet and kyanite. (b) Ti-in-quartz map based on a CL map and quantitative point analyses. (c) Apparent temperature map based on (b), assuming $P = 0.7$ GPa and $aTiO_2 = 1$. (d) Apparent temperature map based on (b), assuming $P = 1.2$ GPa and $aTiO_2 = 1$. (e) Mineral distribution map showing quartz in the matrix and included in kyanite. (f) Ti-in-quartz map based on a CL map and quantitative point analyses. (g) Temperature map assuming $P = 0.7$ GPa and $aTiO_2 = 1$. (h) Temperature map assuming $P = 1.2$ GPa and $aTiO_2 = 1$ [Colour figure can be viewed at wileyonlinelibrary.com]
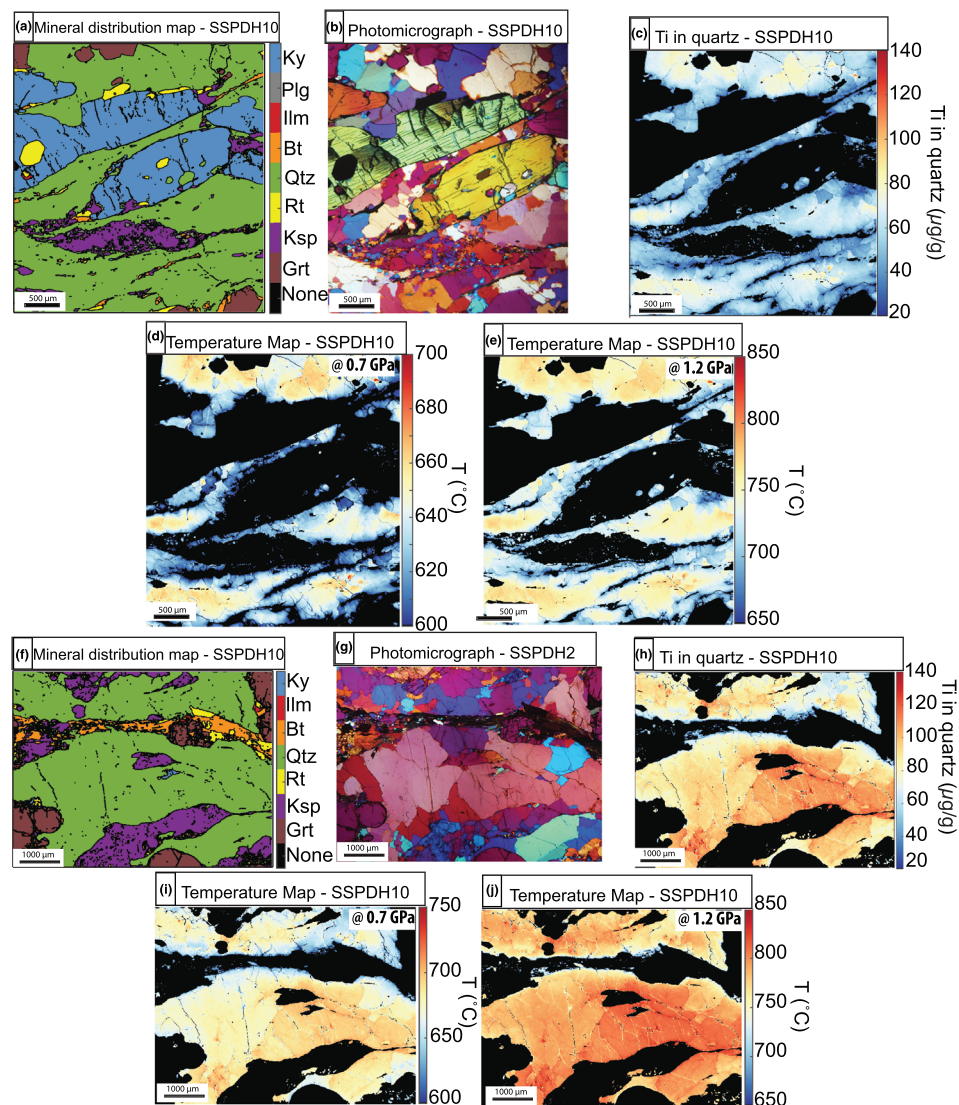
FIGURE 9 Quartz textures and compositions in sample SSPDH10. (a) Mineral distribution map showing the occurrence of quartz in the matrix and included in kyanite. (b) Photomicrograph of mapped area, crossed-polarized light with accessory gypsum plate. (c) Ti-in-quartz map based on a CL map and quantitative point analyses. (d) Apparent temperature map based on (c), assuming $P = 0.7$ GPa and $a\mathrm{TiO}_2 = 1$. (e) Apparent temperature map based on (c), assuming $P = 1.2$ GPa and $a\mathrm{TiO}_2 = 1$. (f) Mineral distribution map showing quartz in the matrix. (g) Photomicrograph of mapped area, crossed-polarized light with accessory gypsum plate. (h) Ti-in-quartz map. (i) Apparent temperature map based on (h), assuming $P = 0.7$ GPa and $a\mathrm{TiO}_2 = 1$. (j) Apparent temperature map based on (f), assuming $P = 1.2$ GPa and $a\mathrm{TiO}_2 = 1$. Abbreviations according to Kretz (1983) [Colour figure can be viewed at wileyonlinelibrary.com]

The biotite forms in the early retrograde reaction at ~800°C in both pseudosections (Figure 10a,c), according to the generalized reaction:

$$\mathrm{Grt + Kfs + Rt + Liq = Bt + Qtz \pm Pl + Ky.}$$
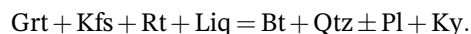
Mineral compositional contours can be used to further constrain the *P-T* conditions of the rock, with zoned porphyroblasts potentially preserving a detailed metamorphic record, if that zoning has been relatively unmodified following initial equilibration.

Grossular content in garnet from SSPDH10 decreases from core to rim (from 0.16 to 0.05; Figure 4d), consistent with progressive growth over evolving *P-T* conditions (Figure 11a,b). Initial growth of garnet at ~650°C and 1.2 GPa (Figure 11a) would result in appropriate core Ca contents, though we note that it is likely that core compositions have been partially modified subsequent to growth, particularly given the subsequent high peak

temperature (Caddick et al., 2010). The decrease of Ca content towards the garnet rim (X_{Grs} down to 0.05) may indicate a post peak decompression of ~0.6 GPa, from ~1.2 to 0.6 GPa (Figure 11b).

Grossular content in garnet from SSPDH2 also decreases from core to center-rim with a slight increase in the external rim (from 0.065 to 0.033 to 0.05 respectively, Figure 4l), despite the zoning not being perfectly concentric in the mapped garnet. The higher grossular content in sample SSPDH2 is consistent with initial garnet growth at prograde conditions of ~600°C and 0.7 GPa (Figure 11d). The lower grossular content of 0.033 represents the peak conditions of 830°C and 1.2 GPa (Figure 11e), and the external rim content of 0.05 is consistent with retrograde conditions of 650°C and 0.75 GPa (Figure 11e), indicating a post peak decompression.

In the pseudosections, relative to the garnet abundance in the peak assemblage field, a decrease in pressure and temperature would result in a decrease in

FIGURE 10 Pressure-temperature (*P-T*) pseudosections calculated in the NCKFMASHTO model chemical system. (a) *P-T* pseudosection calculated by removing the garnet core area from the quantitative map for sample SSPDH10. (b) Melt-reintegrated *P-T* pseudosection calculated by including the previously excluded garnet composition for sample SSPDH10. (c) *P-T* pseudosection calculated by removing the garnet core area from the quantitative map for sample SSPDH2. (d) Melt-reintegrated *P-T* pseudosection calculated by including the previously excluded garnet composition for sample SSPDH2. Quartz is also present in all fields. Compositions shown above diagrams in molar proportion [Colour figure can be viewed at wileyonlinelibrary.com]
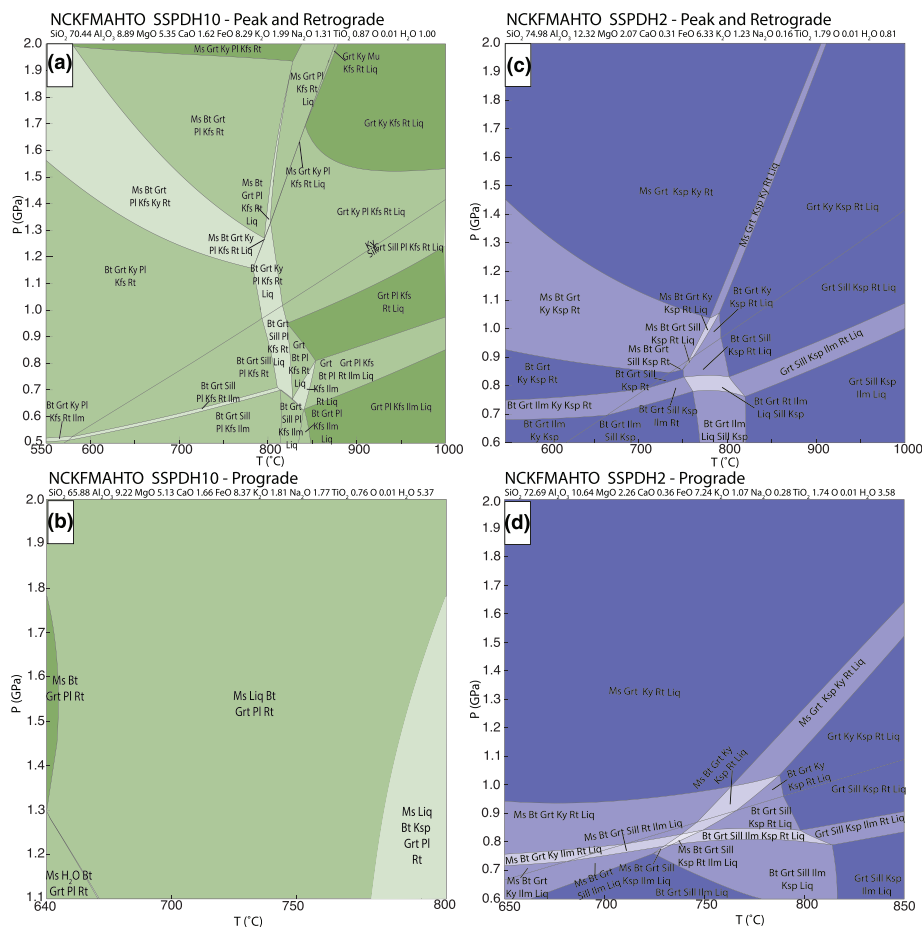
garnet content, whereas garnet content would be relatively constant with isobaric cooling (Figure S3).

4.6 | Monazite U-Th-Pb_T dating

Monazite crystals from samples SSPDH10, SSPDH12, SSPDH2, and MG161 were analyzed (Tables S5 and 5 and Figure 12). In samples SSPDH12 and SSPDH2, the ages of monazite that occur as inclusions in garnet and kyanite overlap with matrix crystal ages within uncertainties, although the monazite inclusions are systematically 9 to 10 myr older than the matrix grains (Figure 12a,b). The same pattern is observed in samples SSPDH10 and MG161, however with a much smaller age difference (<5 Ma, Figure 12c,d). The monazite crystals are commonly zoned in Y, Pb, Ca, and Th. This feature is concentric in some crystals and irregular in others. However, there is no clear correlation between the chemical zoning and dates.

In sample SSPDH12, 36 analyses from eight crystals from the matrix yield a date of 630.9 ± 3.7 Ma, and 39 analyses in seven crystals included in garnet yield a date of 638.9 ± 4.9 Ma (Figure 12a). In sample SSPDH2,

a date of 623.2 ± 7.9 Ma is calculated from four analyzed crystals (28 single dates) in the matrix, and a date of 632.6 ± 5.6 Ma is obtained from monazite grains included in garnet (4 crystals and 21 spots). A younger date of 615 ± 14 Ma was obtained for a monazite crystal included in kyanite (four spots; Figure 12b). Monazite from the matrix of sample SSPDH10 yields a date of 634.7 ± 7.6 Ma (8 crystals and 22 analyses), with inclusions in garnet yielding a date of 640 ± 10 Ma (five crystals and five analyses; Figure 12c). In sample MG161, monazite from the matrix yields a date of 630.9 ± 3.2 Ma (from 52 dates of 11 crystals), while crystals included in garnet yield a date of 633.3 ± 4.9 (36 analyses in eight crystals; Figure 12d).

4.7 | Rutile U-Pb dating

A total of 29 single-spot U-Pb analyses from three samples (SSPDH10, MG161, and SSPDH12) were carried out by LA-ICP-MS (Figure 13d-I and Tables 5 and S6). U-Pb rutile dates in all analyzed samples, in the matrix and as inclusions are similar and significantly younger than the U-Pb-Th_T monazite dates. Concordia ages were
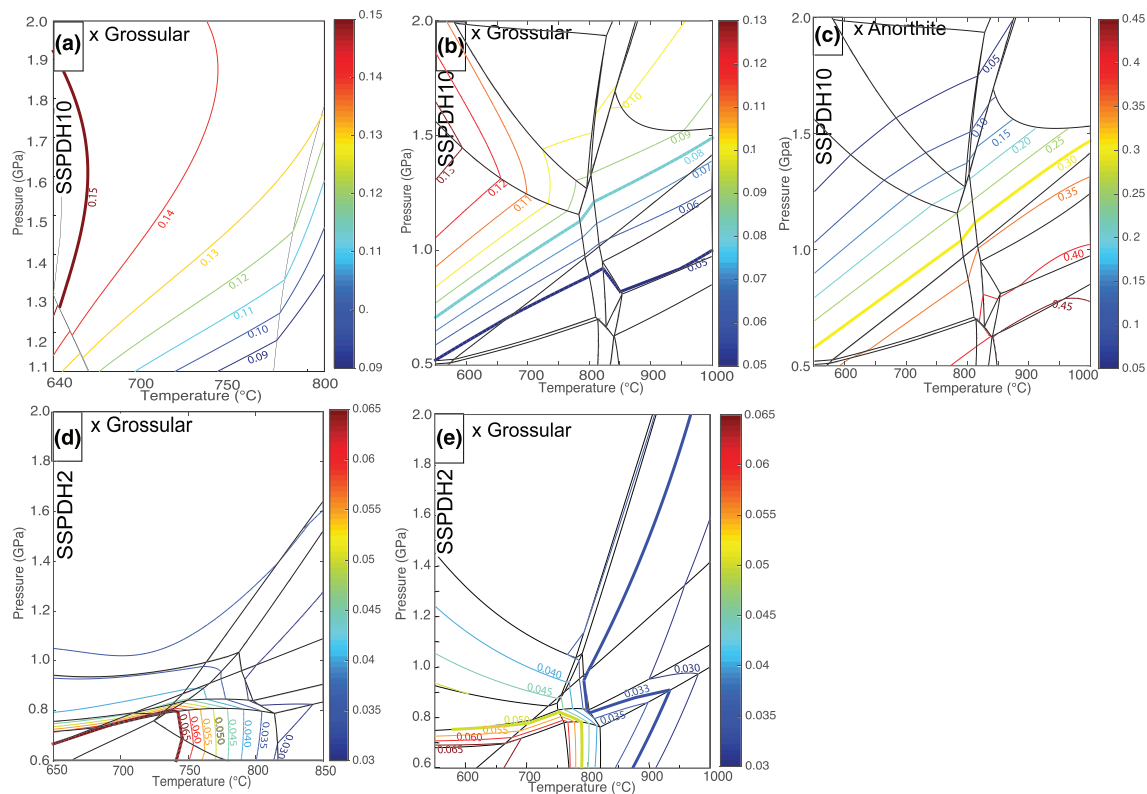
FIGURE 11 Isopleths of grossular content of garnet (Ca/Ca + Fe + Mg + Mn) and of anorthite content of plagioclase. (a) Isopleths of grossular in the *P-T* pseudosection calculated by removing the garnet core area from the quantitative map for sample SSPDH10. (b) Isopleths of grossular in the melt-reintegrated *P-T* pseudosection calculated by including the previously excluded garnet composition for sample SSPDH10. (c) Isopleth of anorthite in the melt-reintegrated *P-T* pseudosection calculated by including the previously excluded garnet composition for sample SSPDH10. (d) Isopleths of grossular in the *P-T* pseudosection calculated by removing the garnet core area from the quantitative map for sample SSPDH2. (e) Isopleth of grossular in melt-reintegrated *P-T* pseudosection calculated by including the previously excluded garnet composition for sample SSPDH2. Calculated mineral compositions for samples SSPDH10 and SSPDH2 are shown on Figure 10 [Colour figure can be viewed at wileyonlinelibrary.com]

calculated at 590.4 ± 4.5 Ma in sample MG161 (MSWD = 0.40), 590.8 ± 6.1 Ma in sample SSPDH10 (MSWD = 0.18) and 585.7 ± 7.5 Ma in sample SSPDH12 (MSWD = 1.8; Figure 13a–c).

5 | DISCUSSION

5.1 | Rutile thermometry interpretations

It has previously been shown that the Zr contents of populations of rutile crystals from granulite facies rocks commonly exhibit large spreads (e.g., Ewing et al., 2013; Hart et al., 2018; Kooijman et al., 2012; Luvizotto & Zack, 2009; Pauly et al., 2016). This is also true for the data presented here, where Zr contents vary from 407 to 1847 μg/g. Although there is no consensus as to what grains and analyses should be used for calculating the temperature of the metamorphic peak, several works agree that part of the high-*T* record is retained in high Zr

content crystals (e.g., Clark et al., 2019; Ewing et al., 2013; Hart et al., 2018; Kohn et al., 2016; Kooijman et al., 2012; Pape et al., 2016; Pauly et al., 2016; Taylor-Jones & Powell, 2015). In an attempt to constrain the conditions of granulite facies metamorphism, and following the recommendation of Luvizotto and Zack (2009) and Hart et al. (2018), we used Zr contents above the 90th percentile to calculate temperature.

Considering only the values are above the 90th percentile, calculated temperatures range from 821°C to 834°C, assuming pressure of 1.2 GPa as constrained by the peak assemblage (Figure 10). These are interpreted as the minimum peak temperature, since we cannot determine the extent to which rutile composition has been modified after its crystallization, but are consistent with the peak assemblage in the pseudosections calculated for samples SSPDH10 and SSPDH2 (Figure 14).

Zircon, rutile, and quartz are present in all textural domains in the rock (i.e., in the melanosome, in the leucosome and in inclusions in garnet and kyanite).

TABLE 5 Summary of rutile and monazite dating data from samples SSPDH12, SSPDH2, MG161, and SSPDH10

Sample	Mineral	Texture	Y_2O_3	SiO_2	ThO_2	CaO	La_2O_3	Ce_2O_3	Pr_2O_3	Nd_2O_3	Sm_2O_3
SSPDH12	Mnz	Incl Grt	0.39	0.16	4.61	0.96	14.29	31.97	3.17	13.22	1.94
SSPDH12	Mnz	Mtx	BD	0.28	4.73	0.91	14.80	31.86	3.19	12.35	1.99
SSPDH12	Mnz	Mtx	BD	0.31	5.02	0.86	15.58	32.10	3.16	12.15	1.90
SSPDH12	Mnz	Incl Grt	0.11	0.29	5.73	1.13	14.61	31.18	3.02	12.37	1.99
SSPDH12	Mnz	Incl Grt	1.06	2.72	11.28	0.12	7.38	26.45	3.61	15.81	4.66
SSPDH12	Mnz	Incl Grt	0.76	1.39	7.73	0.39	14.11	30.77	3.34	11.35	2.45
SSPDH12	Mnz	Mtx	0.71	0.04	4.24	1.08	14.14	30.89	3.06	12.04	2.24
SSPDH12	Mnz	Mtx	2.17	0.07	2.28	0.52	14.08	30.81	3.01	12.89	2.38
SSPDH2	Mnz	Mtx	1.27	0.06	3.93	0.92	15.17	30.96	3.15	12.32	2.01
SSPDH2	Mnz	Mtx	0.20	0.19	4.72	1.23	14.73	31.67	3.10	12.01	1.96
SSPDH2	Mnz	Incl Ky	0.75	0.04	3.71	0.89	13.49	30.85	3.12	13.05	2.56
SSPDH2	Mnz	Incl Ky	0.75	0.04	3.18	0.82	13.25	30.50	3.09	13.40	2.99
SSPDH2	Mnz	Incl Ky	1.10	0.06	3.28	0.80	14.93	31.88	2.88	12.41	1.95
SSPDH2	Mnz	Incl Ky	0.28	0.10	3.66	0.84	14.30	32.25	3.02	12.55	2.19
SSPDH2	Mnz	Incl Grt	0.30	BD	2.07	0.49	17.08	33.67	3.10	11.60	1.72
SSPDH2	Mnz	Incl Grt	0.26	0.16	4.35	1.00	14.39	31.68	2.79	12.51	2.36
SSPDH2	Mnz	Incl Grt	0.43	0.10	4.39	1.18	14.32	31.23	3.08	12.54	2.19
SSPDH2	Mnz	Incl Grt	1.10	0.04	3.91	1.02	13.95	30.91	2.88	11.90	2.07
SSPDH2	Mnz	Incl Bt	1.14	0.09	3.97	0.90	13.85	31.58	2.95	12.53	2.28
SSPDH2	Mnz	Mtx	0.56	0.05	6.39	1.52	13.66	29.91	3.13	11.88	2.09
SSPDH10	Mnz	Mtx	BD	0.26	6.14	1.32	14.45	32.47	3.23	12.48	1.78
SSPDH10	Mnz	Incl Grt	0.18	0.17	4.63	1.08	14.66	31.72	3.32	12.78	1.89
SSPDH10	Mnz	Mtx	0.03	0.27	6.11	1.39	14.15	31.66	3.32	12.52	1.72
SSPDH10	Mnz	Mtx	0.15	0.48	6.26	1.26	15.51	31.13	2.83	11.49	1.62
SSPDH10	Mnz	Incl Grt	0.06	0.11	2.49	0.58	15.22	34.29	3.48	13.64	1.57
SSPDH10	Mnz	Incl Grt	0.06	0.14	3.35	0.86	14.80	32.71	3.17	13.06	1.80

TABLE 5 (Continued)

Sample	Mineral	Texture	Y_2O_3	SiO_2	ThO_2	CaO	La_2O_3	Ce_2O_3	Pr_2O_3	Nd_2O_3	Sm_2O_3
SSPDH10	Mnz	Incl Grt	0.07	0.08	2.01	0.63	15.27	34.20	3.30	13.29	1.72
SSPDH10	Mnz	Mtx	0.08	0.05	0.71	0.33	14.87	33.75	3.39	14.15	1.80
MG161	Mnz	Incl Grt	0.11	BD	2.40	0.46	18.26	35.50	2.95	10.98	0.97
MG161	Mnz	Mtx	0.09	0.21	5.40	1.84	15.49	31.42	2.95	11.59	1.41
MG161	Mnz	Mtx	0.04	0.48	7.17	1.22	15.69	31.42	2.78	11.35	1.29
MG161	Mnz	Incl Grt	0.03	1.20	10.57	1.27	14.78	30.42	2.83	10.67	1.19
MG161	Mnz	Incl Grt	0.08	0.86	9.22	1.31	15.80	30.27	2.70	10.98	1.40
MG161	Mnz	Incl Grt	0.75	1.37	7.70	0.42	14.09	31.02	3.18	11.43	2.32
MG161	Mnz	Mtx	0.80	0.10	4.01	0.95	14.04	30.69	3.11	12.90	2.40
MG161	Mnz	Mtx	0.04	0.68	8.56	1.30	15.02	31.02	2.76	11.08	1.32

TABLE 5 (Continued)

Sample	FeO	Gd_2O_3	Tb_2O_3	Dy_2O_3	UO_2	SO_3	P_2O_5	PbO	Total	Calc	2Sig
SSPDH12	0.10	1.21	BD	BD	0.27	BD	29.46	0.16	102.11	639	28
SSPDH12	BD	0.72	BD	BD	0.74	BD	29.37	0.20	101.32	644	22
SSPDH12	0.07	0.50	BD	BD	0.69	BD	29.14	0.20	101.46	631	22
SSPDH12	0.07	0.84	BD	BD	0.76	BD	29.76	0.19	102.01	669	27
SSPDH12	BD	2.30	BD	BD	0.98	BD	25.28	0.32	102.43	616	20
SSPDH12	BD	1.15	BD	BD	0.23	0.05	27.55	0.21	102.08	640	18
SSPDH12	BD	1.56	BD	BD	0.72	0.09	29.83	0.20	101.13	594	25
SSPDH12	BD	1.87	BD	0.65	0.53	BD	29.76	0.14	101.50	632	19
SSPDH2	BD	1.59	BD	0.64	0.34	BD	29.55	0.15	102.54	619	26
SSPDH2	BD	1.10	BD	BD	0.25	0.37	29.25	0.16	101.34	588	29
SSPDH2	BD	1.93	BD	BD	0.35	0.05	29.61	0.14	101.13	611	29
SSPDH2	BD	2.77	BD	0.48	0.22	0.05	29.58	0.11	101.06	637	29
SSPDH2	BD	1.69	BD	BD	0.29	0.06	29.57	0.13	101.73	605	28
SSPDH2	0.14	1.51	BD	BD	0.29	0.13	29.85	0.13	101.53	610	29
SSPDH2	0.18	0.94	BD	BD	0.37	0.05	30.03	0.09	101.88	631	29
SSPDH2	0.39	1.49	BD	BD	0.25	0.12	29.51	0.15	101.63	637	26
SSPDH2	0.29	1.42	BD	BD	0.52	0.22	29.22	0.17	101.65	607	44

TABLE 5 (Continued)

Sample	FeO	Gd$_2$O$_3$	Tb$_2$O$_3$	Dy$_2$O$_3$	UO$_2$	SO$_3$	P$_2$O$_5$	PbO	Total	Calc	2Sig
SSPDH2	0.05	1.67	BD	0.54	0.57	BD	29.45	0.17	100.46	**634**	21
SSPDH2	BD	1.71	BD	BD	0.76	0.04	29.31	0.15	101.85	**622**	27
SSPDH2	BD	1.21	BD	BD	0.67	0.11	29.14	0.26	100.76	**656**	18
SSPDH10	BD	0.60	BD	BD	0.20	0.17	29.12	0.20	102.19	**631**	25
SSPDH10	BD	0.94	BD	BD	0.56	BD	28.97	0.19	101.03	**634**	24
SSPDH10	0.20	0.51	BD	BD	0.17	0.18	28.96	0.19	101.34	**584**	49
SSPDH10	BD	0.74	BD	BD	0.70	BD	26.05	0.25	98.34	**664**	27
SSPDH10	BD	0.59	BD	BD	0.16	0.13	29.18	0.08	101.44	**637**	23
SSPDH10	BD	0.59	BD	BD	0.16	0.13	28.36	0.11	99.26	**651**	21
SSPDH10	BD	0.75	BD	BD	0.18	0.18	29.15	0.07	101.05	**626**	25
SSPDH10	0.07	0.83	BD	BD	0.22	0.14	29.53	0.04	100.07	**637**	20
MG161	BD	BD	BD	BD	0.07	BD	29.55	0.08	101.74	**632**	15
MG161	BD	0.59	BD	BD	0.30	0.57	28.90	0.18	101.55	**665**	17
MG161	BD	0.52	BD	BD	1.17	BD	28.68	0.22	101.99	**630**	18
MG161	BD	0.46	BD	BD	0.22	BD	27.53	0.32	101.31	**596**	22
MG161	BD	BD	BD	BD	0.22	BD	28.23	0.28	101.89	**632**	18
MG161	BD	1.21	BD	BD	0.25	0.04	27.24	0.20	101.33	**649**	26
MG161	BD	1.84	BD	BD	0.52	BD	29.33	0.17	101.30	**598**	27
MG161	BD	BD	BD	BD	0.22	BD	28.51	0.26	101.30	**631**	24

Sample	Mineral	U	Th	Th/U	ratio 207/235	1 s	ratio 206/238	1 s	rho	ratio 207/206	1 s	age 207/235	1 s	age 206/238	1 s
SSPDH12	Rt	34	<0.009	<0.00030	0.79	0.02	0.0963	0.0019	0.45	0.0594	0.0016	591	13	593	11
SSPDH12	Rt	24	<0.008	<0.00050	0.77	0.02	0.0972	0.0018	0.42	0.0575	0.0016	580	13	598	10
SSPDH12	Rt	27	0.033	0.0012	0.77	0.02	0.0946	0.0017	0.44	0.0594	0.0015	582	12	582	10
SSPDH1A	Rt	27	<0.010	<0.00050	0.76	0.02	0.0937	0.0015	0.41	0.0590	0.0015	575	12	577	9
MG-161	Rt	46	0.020	0.0004	0.80	0.02	0.0951	0.0017	0.47	0.0607	0.0014	594	11	586	10
MG-161	Rt	28	<0.012	<0.00039	0.80	0.02	0.0960	0.0016	0.36	0.0606	0.0017	598	14	591	9
MG-161	Rt	39	<0.011	<0.00021	0.77	0.02	0.0971	0.0016	0.43	0.0576	0.0014	580	12	597	10

(Continues)

TABLE 5 (Continued)

Sample	Mineral	U	Th	Th/U	ratio 207/235	1 s	ratio 206/238	1 s	rho	ratio 207/206	1 s	age 207/235	1 s	age 206/238	1 s
MG-161	Rt	48	<0.012	<0.00023	0.76	0.02	0.0917	0.0017	0.52	0.0598	0.0013	572	10	566	10
SSPDH10	Rt	43	<0.009	<0.00026	0.79	0.02	0.0941	0.0019	0.46	0.0608	0.0015	590	12	579	11
SSPDH10	Rt	35	0.173	0.0049	0.76	0.02	0.0940	0.0017	0.41	0.0587	0.0014	575	11	579	10
SSPDH10	Rt	34	0.009	0.0003	0.80	0.02	0.0949	0.0018	0.48	0.0613	0.0013	598	10	584	11
SSPDH10	Rt	34	<0.009	<0.00028	0.82	0.02	0.0991	0.0020	0.45	0.0598	0.0016	607	13	609	12
SSPDH10	Rt	46	<0.009	<0.00021	0.78	0.02	0.0970	0.0018	0.42	0.0583	0.0014	586	11	597	11

Note: Values in µg/g.

Abbreviations: Meas, measured; rho, error correlation coefficient; 1s, 1 sigma error; 2Sig, 2 sigma error.

Therefore, it can be assumed that the Zr, Ti, and Si system were buffered during the entire *P-T*-t path.

To give some constraint on rutile crystallization conditions, the modal proportions of rutile and biotite have been calculated for samples SSPDH10 and SSPDH2 (Figure S5). We note that sample SSPDH2 is richer in Ti (1.23 wt% TiO_2—XRF whole rock composition) than the other samples (0.91–0.96 wt% TiO_2; Table S4) but that it contains less Mg (1.88 wt% MgO vs. 2.12–3.94 wt% MgO; Table S4). Therefore, modal proportions of biotite are higher in the calculated pseudosections (Figure S5b,f), for prograde and peak conditions, for sample SSPDH10 (up to 15 vol%) than for sample SSPDH2 (up to 0.6 vol%). The opposite behavior is observed for rutile: calculated modal proportions (Figure S5d,h) are lower for sample SSPDH10 (up to 0.07 vol%) than sample SSPDH2 (up to 1.5 vol%). In sample SSPDH2, ilmenite is stable in the pseudosections calculated for the prograde and peak stages (Figure 10c). Comparing the rutile and ilmenite modal proportions (Figure S5h), it is apparent that rutile crystallizes at the expense of ilmenite in sample SSPDH2. We note that the ilmenite-out reaction is strongly pressure dependent (∼0.7–0.8 GPa in Figure 10d) and, according to our modeling, rutile crystallized within a narrow *P* window during the prograde path. The breakdown of biotite has practically no influence on the modal proportion of rutile for sample SSPDH2. Modal proportions calculated for sample SSPDH10 (Figure S5d) indicate that rutile crystallizes at the expense of biotite in this sample. Furthermore, the modal proportions of rutile rapidly increase with the increase of *T* within the field Ms + Liq + Bt + Ksp + Grt + Pl + Rt (Figure S5d,h), indicating prograde growth of rutile. We also note that the biotite-out reaction is strongly temperature dependent (∼810°C at 1.2 GPa; Figure 10a), indicating that no rutile can be formed via biotite breakdown above this temperature. Since high temperatures are recorded by rutile thermometry in all studied samples (up to 837°C), recrystallization may have taken place, allowing for changes in the composition of rutile.

5.2 | Quartz thermometry interpretations

The spread in Ti contents of quartz is large, with an overall variation from 23 to 134 µg/g (Figures 7–9 and 14). Therefore, a careful evaluation of the data combined with a detailed micro-textural study is required to extract meaningful temperatures with Ti-in-quartz thermometry. In this respect, detailed CL mapping is essential, as previously highlighted by Kendrick and Indares (2018a). The quantified Ti maps, based on the CL maps
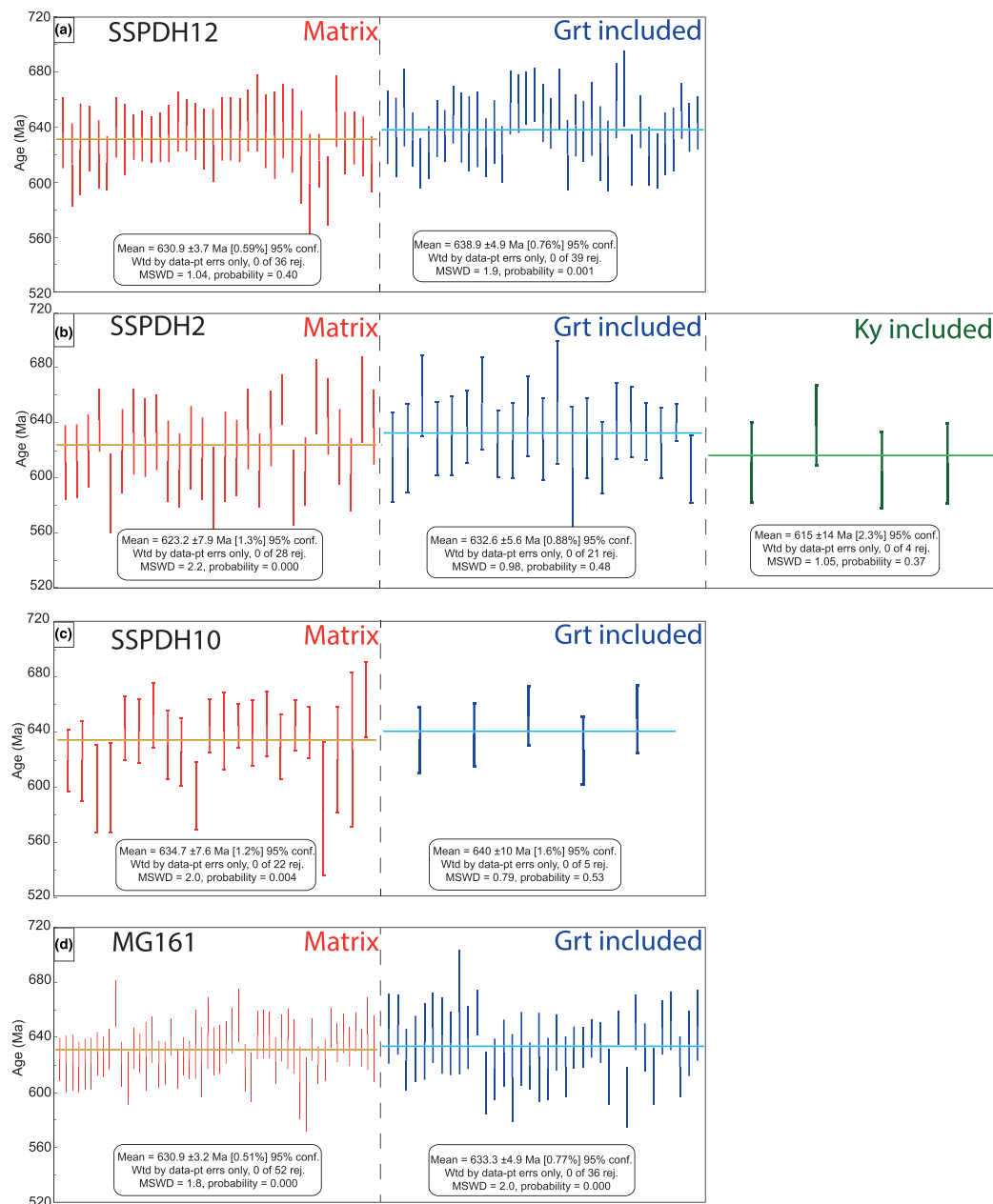
FIGURE 12 Error-weighted average of U-Th-Pb$_T$ EPMA ages of monazite. The diagrams are organized by sample and by monazite textural setting. Horizontal lines show the mean values. Data-point error symbols are all in 2 sigma. Wtd, weighted; conf., confidence; rej., rejected; and MSWD, Mean Square of Weighted Derivates [Colour figure can be viewed at wileyonlinelibrary.com]

(Figures 8 and 9), show extremely heterogeneous distribution of the Ti contents in quartz, with concentrations decreasing from core to rim.

The Ti-in-quartz geothermometer is strongly P dependent (Thomas et al., 2010), so choosing an appropriate P is key. Furthermore, it has been shown that Ti incorporation in quartz is sensitive to post-peak P and T variations (e.g., Nachlas & Hirth, 2015; Thomas et al., 2015) and that dynamic recrystallization enhances the kinetics of Ti equilibration in quartz (Grujic et al., 2011; Kohn & Northrup, 2009; Nachlas &

Hirth, 2015), favoring post crystallization modification of quartz compositions. According to Korchinski et al. (2012), the preservation of high Ti contents in quartz depends on cooling rates and recrystallization, where rapid cooling rates or slow recrystallization favor preservation of early high-Ti grains.

In Figure 9g,h, large quartz grains tend to contain higher Ti contents than smaller grains. Furthermore, lower Ti contents are observed in the outer rim as well as in fractures along the crystals. Using these textural-compositional relationships, large quartz crystals with
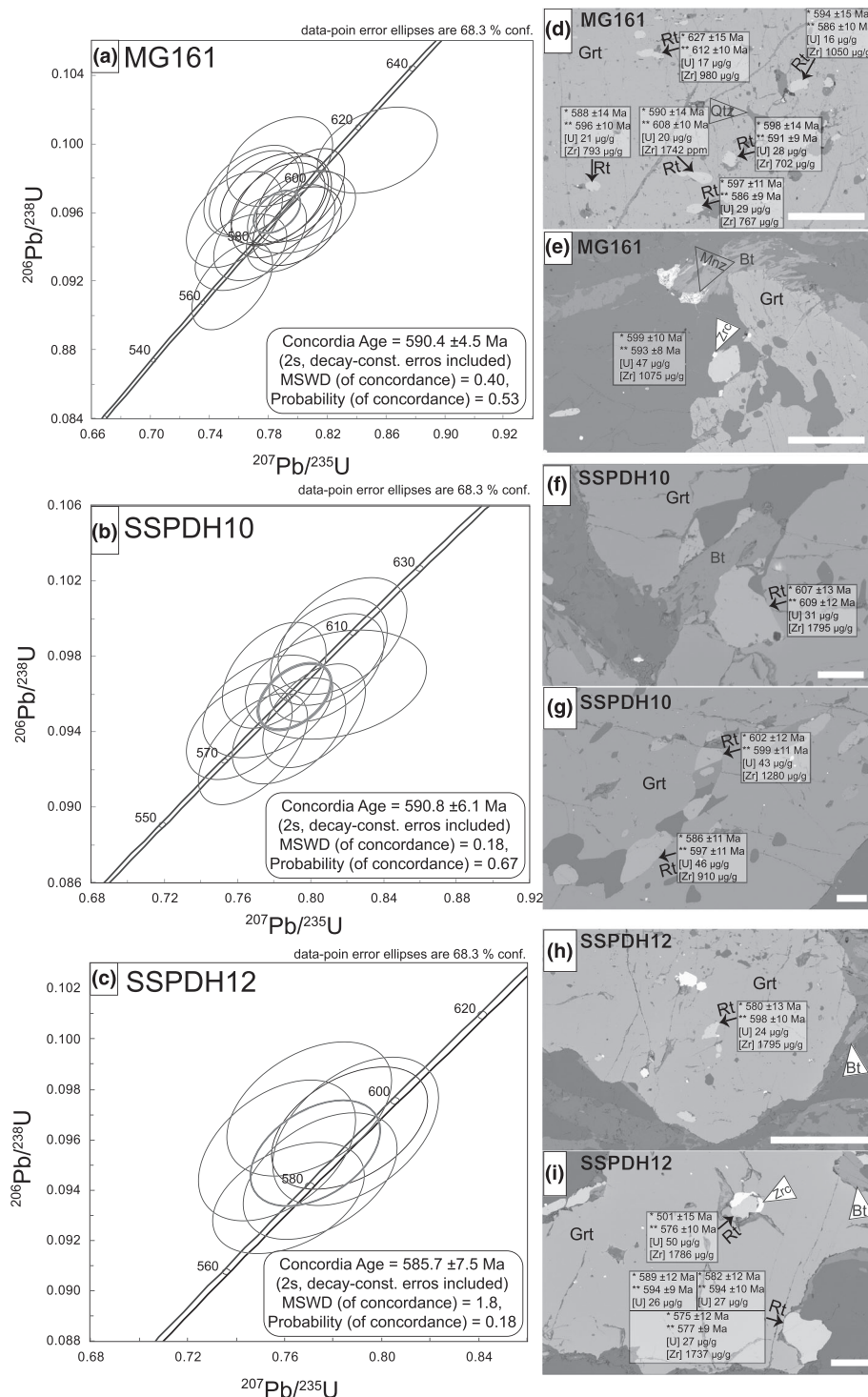
FIGURE 13 U-Pb rutile dating. (a–c) Concordia plot for LA-ICP-MS U-Pb rutile data from samples MG161 (a), SSPDH10 (b), and SSPDH12 (c). MSWD, Mean Square of Weighted Derivates. (d–i) BSE images from the dated rutile with the $^{206}U/^{238}Pb$ age (*), $^{207}U/^{235}Pb$ age (**), and the U and Zr content in the analyzed rutile crystals

high Ti cores are interpreted as a peak phase. The temperature calculated for the high Ti domains is consistent with that of the peak field in the pseudosection modeling as well as the temperature calculated using the highest Zr content in rutile. Hence, the highest Ti contents are interpreted to represent the *T* of melt crystallization shortly after the metamorphic peak. Low Ti contents at the rim of large quartz crystals and in small grains are attributed to post crystallization changes associated with dynamic recrystallization, mostly by grain boundary migration and less frequently by bulging recrystallization. Figure 9b,c shows that the lower Ti contents of quartz are strongly associated with recrystallized portions. This recrystallization is probably associated with the cooling and transport of the Passos Nappe to shallower depths during the later stages of the *P-T*-t path. Kendrick and Indares (2018a) also noted that two populations of quartz occur in aluminous granulites: (i) recrystallized or
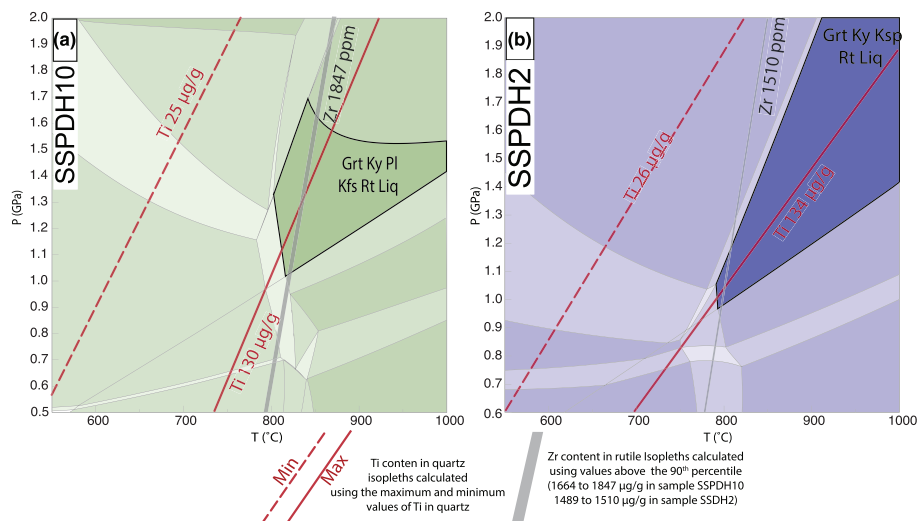
resorbed quartz relics (Ti-rich cores), interpreted to have formed during prograde metamorphism, and (ii) quartz with Ti-poor rims, interpreted to have crystallized from melt. The textures and the variation in Ti content in quartz are similar to those in the present study, though we present an alternative interpretation.

In order to show the effect of P on the apparent temperature, and how an inappropriate P estimate would bias interpretations, T calculations were performed for a peak P of 1.2 GPa, based on pseudosection results for SSPDH10 and SSPDH2 (peak assemblage in Figure 10a,c), and for the estimated retrograde P conditions (grossular core compositions of 0.05; at ~0.7 GPa, Figure 11b,e). For peak P, the results reach 837°C, while at 0.7 GPa, the results would range from ~555°C to 719°C (Figures 8 and 9 and Table 4). The highest T calculated for 1.2 GPa is in good agreement with peak conditions constrained using the pseudosection (Figure 10). The temperatures calculated with the lower contents of Ti-in-quartz, using 0.7 GPa, are interpreted to represent retrograde stage and are consistent with the P-T conditions of the crystallization of ilmenite and biotite, as well as the grossular contents of garnet rims.

5.3 | Petrochronology: Monazite and rutile ages

Monazite is known to record multiple parts of P-T-t paths (Engi, 2017; Foster et al., 2002, 2004; Lanari & Engi, 2017; Montel et al., 2000; Rubatto et al., 2013; Williams et al., 2007, 2017). The older dates found in our study are recorded by monazite crystals included in garnet (ca. 640 Ma in samples SSPDH12 and SSPDH10 and ca. 633 Ma in samples SSPDH12 and MG161). These dates are interpreted as reflecting prograde or near peak metamorphic conditions. Monazite from the matrix, usually present within the leucosome, yields slightly younger dates, 630 Ma in samples SSPDH12, SSPDH10, and MG161 and ca. 623 Ma in SSPDH2, which probably correlate with melt crystallization. The younger age of 615 Ma in a monazite crystal included in kyanite from sample SSPDH2 can be correlated with the growth of retrograde kyanite. Two kyanite textures are observed in the study (Figure 3a–d). Several generations of kyanite in high-pressure granulite were also observed by Kendrick and Indares (2018b). This younger age was obtained for monazite that is included in a kyanite that is interpreted as post-peak. Kyanite modal proportion increases with decreasing pressure and temperature in the calculated pseudosections (Figure S4a,c). Sample SSPDH2 yields younger ages and has more retrograde features, including more biotite and ilmenite needles in rutile, than other studied samples. These ages thus probably correlate with later processes associated cooling and exhumation to shallower crustal conditions.

The metamorphic peak age of 640–630 Ma is similar to previously presented data for the Passos Nappe (Valeriano, Machado, et al., 2004) and high-pressure mafic granulite lenses in the Andrelândia Nappe System (Coelho et al., 2017, at 625 ± 6 Ma; Frugis et al., 2018, at 635–600 Ma; Tedeschi et al., 2017, at ca. 630 Ma). However, our peak age is older than the thermal peak monazite ages described in the high-pressure granulite in the Andrelândia Nappe System by Campos Neto et al. (2010) and da Motta and Moraes (2017), at 617.7 ± 1.3 Ma and 604.5 ± 6.1 Ma, respectively. It is noteworthy that the U-Pb ID-TIMS monazite concordia age of Campos Neto et al. (2010) was defined by dating seven euhedral up to millimeter-sized monazite crystals that are prevalent in the matrix of the granulite and are typically associated

with retrogressed biotite. They can thus be interpreted as associated with cooling after decompression at 617.7 ± 1.3 Ma (Campos Neto et al., 2010) and not as peak ages. The range of monazite ages from da Motta and Moraes (2017) is similar to the ages presented in this work, suggesting that the interpretation of peak metamorphism at 604.5 ± 6.1 Ma could be inappropriate. The interpretation of retrograde ages of ca. 618 and 604 Ma are in agreement with our data in the Passos Nappe.

Even though rutile is a stable phase at high grade metamorphic conditions, the diffusion rates of trace elements, such as Zr, Pb, Nb, Hf, Nb, and Ta, differ significantly at high *P-T* conditions (e.g., Cherniak, 2000; Cherniak et al., 2007; Dohmen et al., 2019; Marschall et al., 2013). According to Cherniak (2000), the effective closure temperature of Pb in rutile is $\sim$600°C for a 100 μm rutile grain, depending also on cooling rate. This implies that the U-Pb age will record cooling ages at lower crustal conditions, complementing earlier zircon and monazite ages in the same rock (Zack & Kooijman, 2017).

The U-Pb rutile ages obtained in the present study range from 590.8 ± 6.1 Ma (sample SSPDH10) to 585.7 ± 7.5 Ma (sample SSPDH12). These are identical within uncertainties to the TIMS rutile age of ca. 594 Ma obtained by Valeriano, Machado, et al. (2004) for rutile in amphibolite from the Passos Nappe and are also in agreement with a Rb–Sr isochron date of ca. 590 Ma presented by Reno et al. (2009) in the Andrelândia Nappe System. The rutile ages record retrograde stages of the *P-T* path and indicate that the cooling and exhumation of the Passos Nappe to lower/middle crust conditions ($\sim$600°C, closure *T* of U-Pb system in rutile) occurred at ca. 590 Ma. Similar ages and interpretations are also presented for the Andrelândia Nappe System by Reno et al. (2012) and Westin et al. (2021).

5.4 | *P-T*-t path

The data presented here indicate that the studied rocks followed a clockwise *P-T*-t path (Figure 15). The prograde stage is documented by the highest grossular content in garnet cores, up to 0.15 in the sample SSPDH10 and 0.065 in the sample SSPDH2 (Figure 11a,d). It is likely that initial growth compositions were even more calcic and that intra-crystalline diffusion has subsequently modified the crystal core compositions (Baxter et al., 2017; Caddick et al., 2010). However, diffusion was not sufficiently intensive to completely eradicate zoning. Peak metamorphic conditions of $\sim$830°C $\pm$ 30°C and 1.20 GPa, are constrained by (i) the plagioclase composition in sample SSPDH10 (Figure 11c); (ii) the grossular

content in garnet inner rims of 0.08 in sample SSPDH10 and 0.033 in sample SSPDH2 (Figure 11b); (iii) the Zr content in rutile (Figures 6 and 14); and (iv) the highest contents of Ti-in-quartz. Retrograde conditions involved a cooling path with a decompressional initial stage (to $\sim$0.5 GPa and 550°C in sample SSPDH10 and to $\sim$0.7 GPa and 650°C in sample SSPDH2), recorded by (i) the decrease in grossular content of garnet to 0.05 in sample SSPDH10 and the increase to 0.05 in sample SSPDH2 (Figure 11b,e); (ii) the crystallization of biotite; (iii) replacement of rutile by ilmenite; and (iv) lower contents of Ti-in-quartz rims associated with recrystallization. The age of prograde-to-peak metamorphism is constrained by monazite crystals included in garnet at ca. 640–633 Ma. Retrograde conditions of $\sim$680°C and 0.9 GPa are constrained by the age of monazite included in retrograde kyanite at 615 Ma (Figure 15). Rutile ages of ca. 590 Ma indicate further cooling, down to $\sim$600°C (U-Pb closure temperature).

5.5 | Tectonic setting and regional correlation

The clockwise *P-T*-t path indicates that the metamorphic peak occurred in the high-pressure granulite facies (Figure 15), under lower crustal conditions, and was followed by stages of cooling and decompression (Figure 16). This *P-T*-t path reflects a sequence of events from initial subduction of the distal passive margin of the São Francisco paleocontinent, followed by crustal thickening and subsequent exhumation (Figure 16). Our data suggest an intermediate geothermal gradient of 18°C/km or $\sim$690°C/GPa, which is consistent with a continent-continent collisional setting (Brown, 2007; Brown & Johnson, 2018; Sizova et al., 2014). The studied rocks result from the metamorphism of continental margin sediments in the deep root of this Cryogenian-Ediacaran continent-continent collisional zone, at ca. 635 Ma, related with the early phases of West Gondwana formation (Figure 16a). The retrograde path (Figures 15 and 16) records exhumation to $\sim$600°C at < 0.9 GPa at a relatively slow integrated cooling rate, of $\sim$6°C/Ma.

According to O'Brien and Rötzler (2003), high-pressure granulites are formed as a result of short-lived tectonic events that led to crustal thickening or subduction of the crust. They infer that the preservation of prograde zoning in minerals such as garnet is evidence of short durations at high-temperature conditions. Although our data indicate a relatively slow integrated cooling for the high-pressure granulite, garnet zoning is most likely preserved because the total time at or near the highest temperature was relatively short.

FIGURE 15 Pressure-temperature-time (*P-T*-t) path for sample SSPDH10 (a) and SSPDH2 (b), based on constraints from the pseudosection, Zr-in-rutile content (concentrations above the 90th percentile), grossular values, anorthite values, Ti-in-quartz content, U-Pb-Th$_T$ dating in monazite, and U-Pb dating in rutile. Depth (km) according to Bucher and Grapes (2011) [Colour figure can be viewed at wileyonlinelibrary.com]

FIGURE 16 Simplified sketch of the tectonic evolution of the Southern Brasília Orogen at the latitude of the Passos Nappe interpreted in this study at ∼635 Ma (a), ∼615 Ma (b), and ∼590–570 Ma (c). The green star represents the position of the high-pressure granulite of the Passos Nappe [Colour figure can be viewed at wileyonlinelibrary.com]

The slow cooling rates in the high-pressure granulite of the Passos Nappe corroborate previous descriptions of long-lived metamorphism and deformation, which lasted at least 30 my, in the Southern Brasília Orogen more to the south (Cioffi et al., 2019; Coelho et al., 2017; Rocha et al., 2017; Tedeschi et al., 2018; Trouw et al., 2000).

Muscovite K-Ar ages of ca. 570–580 Ma in the Passos Nappe are described by Valeriano et al. (2000) and record the final cooling stages upon exhumation to the upper crust (~300°C). The cooling rate of this final stage of the retrograde *P-T*-t path is faster (~15°C/Ma) than calculated for the earlier phase. Similar exhumation/cooling $^{40}Ar/^{39}Ar$ biotite ages around 590–570 Ma are described in high-pressure granulite from Andrelândia Nappe System (Westin et al., 2021).

High-pressure granulites also occur in the southernmost portion of the Brasília Orogen, in the upper portion of the Andrelândia Nappe System, where rocks reached *P-T* conditions of ~800–850°C and 1.2 to 1.4 GPa (Campos Neto et al., 2000, 2010; Cioffi et al., 2012, 2019; da Motta & Moraes, 2017; Reno et al., 2009, 2012). The metamorphic peak conditions of the rocks from the Andrelândia Nappe System are very similar to those of the top of the Passos Nappe.

Although the present work is the first to systematically investigate the high-pressure granulite from Passos Nappe, a correlation of these rocks with the ones from the Andrelândia Nappe System has previously been presented in the literature (Reno et al., 2012; Trouw et al., 1984). Comparing Passos Nappe high pressure granulites with those from the Andrelândia Nappe System is possible on basis of similar mineral assemblages, similar *P-T* conditions, and similar ages of metamorphic peak and exhumation/colling ages. In the Passos Nappe there is a gradual transition from low grade metamorphism in the lower part to high pressure granulite facies in the upper part, all within a single nappe in which the protoliths are interpreted to be derived from a passive margin sedimentary basin. In the Andrelândia Nappe System there are several nappes that are separated by basement slices and thrust faults. These nappes were originally defined, mapped (Trouw et al., 2000) and stacked based on these structures. Some authors (e.g., Campos Neto et al., 2010; Frugis et al., 2018) interpret these different nappes as being derived from different sedimentary basins; the upper part of the stack would be derived from a fore arc basin related to the upper plate, the active margin of the Paranapanema paleocontinent. However, other authors (e.g., Coelho et al., 2017; Trouw et al., 2013) maintain the interpretation that the whole stack is derived from the passive margin of the São Francisco Paleocontinent, similar to the interpretation of the Passos Nappe presented here. It is, however, noteworthy that the retrograde replacement of kyanite by sillimanite, widely observed in the metasedimentary high-pressure Andrelândia Nappe rocks (Campos Neto et al., 2010; Cioffi et al., 2012; da Motta & Moraes, 2017; Reno et al., 2012; Trouw et al., 2013), is absent in all studied high-pressure granulites from the Passos Nappe and other nappes to the north. The widespread occurrence of late sillimanite in the Andrelândia Nappe System could be explained, at least in part, by the partial superposition of Ribeira Orogen metamorphism on the system (Carvalho et al., 2020; Coelho et al., 2017; Trouw et al., 2013), or just by the following decompression, without the effect of this tectonic superposition (Campos Neto et al., 2010; Cioffi et al., 2012; da Motta & Moraes, 2017). Exhumation of the Passos Nappe may have occurred at slightly higher pressure than the Andrelândia Nappe System, with rocks decompressing and cooling entirely within the kyanite field.

6 | CONCLUSIONS

The combination of petrological modeling, trace element geothermometry, and multi-phase geochronology allows the determination of the *P-T*-t path of high-pressure granulites from the upper Passos Nappe. Both Ti-in-quartz and Zr-in-rutile contents show a large spread, as expected. The highest contents of Zr-in-rutile and Ti-in-quartz record the metamorphic peak conditions. Lower Ti contents in quartz are consistent with retrograde conditions.

The studied samples record a clockwise *P-T*-t path with prograde conditions of ~600°C and 0.7 GPa, peak conditions of ~830°C and 1.2 GPa, and retrograde conditions of ~550°C and 0.5 GPa. The prograde-to-peak metamorphism, inferred from monazite ages, occurred ca. 635 Ma. Rutile U-Pb dating indicates a cooling age to ~600°C at ca. 590 Ma. The metamorphic *P-T* path constrained in this work is consistent with a continental collision setting in the Southern Brasília Orogen and indicates a relatively slow cooling rate for rocks from the top of the Passos Nappe pile. Both the peak *P-T* conditions and metamorphic ages suggest that the high-pressure granulites from the Passos Nappe were involved in similar timing and conditions as the granulites from the Andrelândia Nappe System to the south.

ORCID

Regiane Andrade Fumes https://orcid.org/0000-0003-4055-7906

George Luiz Luvizotto https://orcid.org/0000-0002-6150-8292

Renato Moraes https://orcid.org/0000-0001-6917-3696

Pierre Lanari https://orcid.org/0000-0001-8303-0771

Claudio de Morisson Valeriano https://orcid.org/0000-0002-9341-2615

Thomas Zack https://orcid.org/0000-0003-4747-4134

Mark J. Caddick https://orcid.org/0000-0001-8795-8438

Luiz Sergio Amarante Simões https://orcid.org/0000-0002-5198-8210

REFERENCES

Araújo Filho, J. O. (2000). The Pirineus Syntaxis: An example of the intersection of two brasiliano fold-thrust belts in the central Brasil and its implications for the tectonic evolution of Western Gondwana. *Revista Brasileira de Geociencias*, *30*(1), 144–148. https://doi.org/10.25249/0375-7536.2000301144148

Armstrong, R. L. (1991). A brief history of geochronometry and radiogenic isotopic studies. In L. Heamam & J. N. Ludden (Eds.), *Aplications of Radiogenic Isotope Systems to Problens in Geology* (pp. 1–26). Mineralogical Association of Canada.

Ashley, K. T., & Law, R. D. (2015). Modeling prograde TiO2 activity and its significance for Ti-in-quartz thermobarometry of pelitic metamorphic rocks. *Contributions to Mineralogy and Petrology*, *169*(2), 1–7. https://doi.org/10.1007/s00410-015-1118-7

Audétat, A., Garbe-Schönberg, D., Kronz, A., Pettke, T., Rusk, B., Donovan, J. J., & Lowers, H. A. (2015). Characterisation of a natural quartz crystal as a reference material for microanalytical determination of Ti, Al, Li, Fe, Mn, Ga and Ge. *Geostandards and Geoanalytical Research*, *39*(2), 171–184. https://doi.org/10.1111/j.1751-908X.2014.00309.x

Baldwin, J. A., Powell, R., Brown, M., Moraes, R., & Fuck, R. A. (2005). Modelling of mineral equilibria in ultrahigh-temperature metamorphic rocks from the Anápolis-Itauçu Complex, central Brazil. *Journal of Metamorphic Geology*, *23*(7), 511–531. https://doi.org/10.1111/j.1525-1314.2005.00591.x

Barbosa, O. (1955). Guia das excursões. *Congresso Brasileiro de Geologia*, *9*, 3–5.

Baxter, E. F., Caddick, M. J., & Dragovic, B. (2017). Garnet: A Rock-Forming Mineral Petrochronometer. *Reviews in Mineralogy and Geochemistry*, *83*(1), 469–533.

Brown, M. (2007). Metamorphic Conditions in Orogenic Belts: A Record of Secular Change. *International Geology Review*, *49*(3), 193–234. https://doi.org/10.2747/0020-6814.49.3.193

Brown, M., & Johnson, T. (2018). Secular change in metamorphism and the onset of global plate tectonics. *American Mineralogist*, *103*(2), 181–196. https://doi.org/10.2138/am-2018-6166

Bucher, K., & Grapes, R. (2011). *Petrogenesis of Metamorphic Rocks*. Springer. https://doi.org/10.1007/978-3-540-74169-5

Caddick, M. J., Konopásek, J., & Thompson, A. B. (2010). Preservation of garnet growth zoning and the duration of prograde metamorphism. *Journal of Petrology*, *51*(11), 2327–2347. https://doi.org/10.1093/petrology/egq059

Campos Neto, M. C., Da Costa, M., & Caby, R. (1999). Neoproterozoic high-pressure metamorphism and tectonic constraint from the nappe system south of the Sao Francisco Craton, southeast Brazil. *Precambrian Research*, *97*(1–2), 3–26. https://doi.org/10.1016/S0301-9268(99)00010-8

Campos Neto, M. C., Da Costa, M., & Caby, R. (2000). Lower crust extrusion and terrane accretion in the Neoproterozoic nappes of southeast Brazil. *Tectonics*, *19*, 669–687. https://doi.org/10.1029/1999TC900065

Campos Neto, M. C., da Costa, M., Cioffi, C. R., Moraes, R., da Motta, R. G., Siga, O., & Basei, M. A. S. (2010). Structural and metamorphic control on the exhumation of high-P granulites: The Carvalhos Klippe example, from the oriental Andrelândia Nappe System, southern portion of the Brasília Orogen, Brazil. *Precambrian Research*, *180*(3–4), 125–142. https://doi.org/10.1016/j.precamres.2010.05.010

Campos Neto, M. C., Janasi, V. A., Basei, M. A. S., & Siga, O. Jr. (2007). Sistema de nappes Andrelândia, setor oriental: litoestratigrafia e posição estratigráfica. *Revista Brasileira de Geociencias*, *37*(S4), 47–60. https://doi.org/10.25249/0375-7536.200737s44760

Carvalho, B. R. B. M., Trouw, R. A. J., da Costa, R. V. C., Ribeiro, A., Heilbron, M., & Marimon, R. S. (2020). Microstructural and metamorphic evolution of the Carrancas Klippe, interference zone of the Neoproterozoic southern Brasilia and Ribeira orogens, SE Brazil. *Journal of South American Earth Sciences*, *103*(February), 102744. https://doi.org/10.1016/j.jsames.2020.102744

Cherniak, D. J. (2000). Pb diffusion in rutile. *Contributions to Mineralogy and Petrology*, *139*(2), 198–207. https://doi.org/10.1007/PL00007671

Cherniak, D. J., Watson, E. B., & Wark, D. A. (2007). Ti diffusion in quartz. *Chemical Geology*, *236*(1–2), 65–74. https://doi.org/10.1016/j.chemgeo.2006.09.001

Cioffi, C. R., Campos Neto, M. C., Möller, A., & Rocha, B. C. (2019). Titanite petrochronology of the southern Brasília Orogen basement : Effects of retrograde net-transfer reactions on titanite trace element compositions. *Lithos*, *345*, 393–408. https://doi.org/10.1016/j.lithos.2019.06.035

Cioffi, C. R., Campos Neto, M. d. C., Rocha, B. C. d., Moraes, R., & Henrique-Pinto, R. (2012). Geochemical signatures of metasedimentary rocks of high-pressure granulite facies and their relation with partial melting: Carvalhos Klippe, Southern

Brasília Belt, Brazil. *Journal of South American Earth Sciences*, *40*, 63–76. https://doi.org/10.1016/j.jsames.2012.09.007

Clark, C., Taylor, R. J. M., Johnson, T. E., Harley, S. L., Fitzsimons, I. C. W., & Oliver, L. (2019). Testing the fidelity of thermometers at ultrahigh temperatures. *Journal of Metamorphic Geology*, *37*(7), 917–934. https://doi.org/10.1111/jmg.12486

Coelho, M. B., Trouw, R. A. J., Ganade, C. E., Vinagre, R., Mendes, J. C., & Sato, K. (2017). Constraining timing and P-T conditions of continental collision and late overprinting in the Southern Brasília Orogen (SE-Brazil): U-Pb zircon ages and geothermobarometry of the Andrelândia Nappe System. *Precambrian Research*, *292*, 194–215. https://doi.org/10.1016/j.precamres.2017.02.001

Cruz-Uribe, A. M., Feineman, M. D., Zack, T., & Jacob, D. E. (2018). Assessing trace element (dis)equilibrium and the application of single element thermometers in metamorphic rocks. *Lithos*, *314–315*, 1–15. https://doi.org/10.1016/j.lithos.2018.05.007

da Motta, R. G., & Moraes, R. (2017). Pseudo- and real-inverted metamorphism caused by the superposition and extrusion of a stack of nappes: A case study of the Southern Brasília Orogen, Brazil. *International Journal of Earth Sciences*, *106*(7), 2407–2427. https://doi.org/10.1007/s00531-016-1436-7

Dardenne, M. A. (2000). The Brasilia Fold Belt. In U. G. Cordani, E. J. Milani, A. T. Filho, & D. A. Campos (Eds.), *Tectonic evolution of South America: 31ᵗʰ International Geological Congress* (pp. 231–263).

Dickin, A. P. (1995). *Radiogenic Isotope Geology*. Cambrige University Press.

Dohmen, R., Marschall, H. R., Ludwig, T., & Polednia, J. (2019). Diffusion of Zr, Hf, Nb and Ta in rutile: Effects of temperature, oxygen fugacity, and doping level, and relation to rutile point defect chemistry. *Physics and Chemistry of Minerals*, *46*(3), 311–332.

Engi, M. (2017). Petrochronology Based on REE-Minerals: Monazite, Allanite, Xenotime, Apatite. *Reviews in Mineralogy and Geochemistry*, *83*(1), 365–418. https://doi.org/10.2138/rmg.2017.83.12

Engi, M., Lanari, P., & Kohn, M. J. (2017). Significant Ages — An Introduction to Petrochronology. *Reviews in Mineralogy and Geochemistry*, *83*, 1–10. https://doi.org/10.2138/rmg.2017.83.1

Ewing, T. A., Hermann, J., & Rubatto, D. (2013). The robustness of the Zr-in-rutile and Ti-in-zircon thermometers during high-temperature metamorphism (Ivrea-Verbano Zone, northern Italy). *Contributions to Mineralogy and Petrology*, *165*(4), 757–779. https://doi.org/10.1007/s00410-012-0834-5

Foster, G., Parrish, R. R., Horstwood, M. S. A., Chenery, S., Pyle, J., & Gibson, H. D. (2004). The generation of prograde P-T-t points and paths; a textural, compositional, and chronological study of metamorphic monazite. *Earth and Planetary Science Letters*, *228*(1–2), 125–142, 142. https://doi.org/10.1016/j.epsl.2004.09.024

Foster, Gavin, Gibson, H. D., Parrish, R., Horstwood, M., Fraser, J., & Tindle, A. (2002). Textural, chemical and isotopic insights into the nature and behaviour of metamorphic monazite. *Chemical Geology*, *191*(1–3), 183–207. https://doi.org/10.1016/S0009-2541(02)00156-0, 183

Frugis, G. L., Campos Neto, M. C., & Lima, R. B. (2018). Eastern Paranapanema and southern São Francisco orogenic margins:

Records of enduring Neoproterozoic oceanic convergence and collision in the southern Brasília Orogen. *Precambrian Research*, *308*(February), 35–57. https://doi.org/10.1016/j.precamres.2018.02.005

Fuck, R. A., Pimentel, M. M., Alvarenga, C. J. S., & Dantas, E. L. (2017). The Northern Brasília Belt. In M. Heilbron, U. Cordani, & F. F. Alkimin (Eds.), *São Francisco Craton, Eastern Brazil. Regional Geology Reviews* (pp. 205–220). Springer International Publishing. https://doi.org/10.1007/978-3-319-01715-0_11

Fuck, R. A., Pimentel, M. M., & Silva, L. J. H. D. (1994). Compartimentação tectônica da porção oriental da Província Tocantins. In: *Congresso Brasileiro de Geologia* (Vol. 38, pp. 215–216). SBG Balneário Camboriú.

Gebauer, D., & Grünenfelder, M. (1979). U-Th-Pb dating of minerals. In *Lectures in isotope geology* (pp. 105–131). Springer. https://doi.org/10.1007/978-3-642-67161-6_7

Gonçalves, G. O., Lana, C., Scholz, R., Buick, I. S., Gerdes, A., Kamo, S. L., Corfu, F., Marinho, M. M., Chaves, A. O., Valeriano, C., & Nalini, H. A. (2016). An assessment of monazite from the Itambé pegmatite district for use as U-Pb isotope reference material for microanalysis and implications for the origin of the "Moacyr" monazite. *Chemical Geology*, *424*, 30–50. https://doi.org/10.1016/j.chemgeo.2015.12.019

Grujic, D., Stipp, M., & Wooden, J. L. (2011). Thermometry of quartz mylonites: Importance of dynamic recrystallization on Ti-in-quartz reequilibration. *Geochemistry, Geophysics, Geosystems*, *12*(6), 1–19. https://doi.org/10.1029/2010GC003368

Hart, E., Storey, C., Harley, S. L., & Fowler, M. (2018). A window into the lower crust: Trace element systematics and the occurrence of inclusions/intergrowths in granulite-facies rutile. *Gondwana Research*, *59*, 76–86. https://doi.org/10.1016/j.gr.2018.02.021

Holland, T. J. B., & Powell, R. (2011). An improved and extended internally consistent thermodynamic dataset for phases of petrological interest, involving a new equation of state for solids. *Journal of Metamorphic Geology*, *29*(3), 333–383. https://doi.org/10.1111/j.1525-1314.2010.00923.x

Indares, A., White, R. W., & Powell, R. (2008). Phase equilibria modelling of kyanite-bearing anatectic paragneisses from the central Grenville Province. *Journal of Metamorphic Geology*, *26*(8), 815–836. https://doi.org/10.1111/j.1525-1314.2008.00788.x

Kendrick, J., & Indares, A. (2018a). The reaction history of kyanite in high- P aluminous granulites. *Journal of Metamorphic Geology*, *36*, 125–146. https://doi.org/10.1111/jmg.12286

Kendrick, J., & Indares, A. (2018b). The Ti record of quartz in anatectic aluminous granulites. *Journal of Petrology*, *59*(8), 1493–1516. https://doi.org/10.1093/petrology/egy070

Kidder, S., Avouac, J. P., & Chan, Y. C. (2013). Application of titanium-in-quartz thermobarometry to greenschist facies veins and recrystallized quartzites in the Hsüehshan range, Taiwan. *Solid Earth*, *4*(1), 1–21. https://doi.org/10.5194/se-4-1-2013

Kohn, M. J., & Northrup, C. J. (2009). Taking mylonites' temperatures. *Geology*, *37*(1), 47–50. https://doi.org/10.1130/G25081A.1

Kohn, M. J., Penniston-Dorland, S. C., & Ferreira, J. C. S. (2016). Implications of near-rim compositional zoning in rutile for geothermometry, geospeedometry, and trace element

equilibration. *Contributions to Mineralogy and Petrology*, *171*(10), 1–15. https://doi.org/10.1007/s00410-016-1285-1

Kooijman, E., Smit, M. A., Mezger, K., & Berndt, J. (2012). Trace element systematics in granulite facies rutile: Implications for Zr geothermometry and provenance studies. *Journal of Metamorphic Geology*, *30*(4), 397–412. https://doi.org/10.1111/j.1525-1314.2012.00972.x

Korchinski, M., Little, T. A., Smith, E., & Millet, M. A. (2012). Variation of Ti-in-quartz in gneiss domes exposing the world's youngest ultrahigh-pressure rocks, D'Entrecasteaux Islands, Papua New Guinea. *Geochemistry, Geophysics, Geosystems*, *13*(1), 1–27. https://doi.org/10.1029/2012GC004230

Kretz, R. (1983). Symbols for rock-forming. *American Mineralogist*, *68*, 277–279.

Lanari, P., & Engi, M. (2017). Local Bulk Composition Effects on Metamorphic Mineral Assemblages. *Reviews in Mineralogy and Geochemistry*, *83*, 55–93. https://doi.org/10.2138/rmg.2017.83.3

Lanari, P., Vho, A., Bovay, T., Airaghi, L., & Centrella, S. (2019). Quantitative compositional mapping of mineral phases by electron probe micro-analyser. *Geological Society Special Publication*, *478*(1), 39–63. https://doi.org/10.1144/SP478.4

Lanari, P., Vidal, O., De Andrade, V., Dubacq, B., Lewin, E., Grosch, E. G., & Schwartz, S. (2014). XMapTools: A MATLAB©-based program for electron microprobe X-ray image processing and geothermobarometry. *Computers and Geosciences*, *62*, 227–240. https://doi.org/10.1016/j.cageo.2013.08.010

Lasalle, S., & Indares, A. (2014). Anatectic record and contrasting P-T paths of aluminous gneisses from the central Grenville Province. *Journal of Metamorphic Geology*, *32*(6), 627–646. https://doi.org/10.1111/jmg.12083

Leeman, W. P., MacRae, C. M., Wilson, N. C., Torpy, A., Lee, C. T. A., Student, J. J., Thomas, J. B., & Vicenzi, E. P. (2012). A study of cathodoluminescence and trace element compositional zoning in natural quartz from volcanic rocks: Mapping titanium content in quartz. *Microscopy and Microanalysis*, *18*(6), 1322–1341. https://doi.org/10.1017/S1431927612013426

Ludwig, K. R. (2003). Isoplot 3.00: A geochronological toolkit for Microsoft Excel. *Berkeley Geochronology Center Special Publication*, *4*, 70.

Luvizotto, G. L. (2003). *Caracterização metamórfica das rochas do Grupo Araxá na região de São Sebastião do Paraíso, sudoeste de Minas Gerais*. Universidade Estadual Paulista.

Luvizotto, G. L., & Zack, T. (2009). Nb and Zr behavior in rutile during high-grade metamorphism and retrogression: An example from the Ivrea-Verbano Zone. *Chemical Geology*, *261*(3–4), 303–317. https://doi.org/10.1016/j.chemgeo.2008.07.023

Luvizotto, G. L., Zack, T., Meyer, H. P., Ludwig, T., Triebold, S., Kronz, A., Münker, C., Stockli, D. F., Prowatke, S., Klemme, S., Jacob, D. E., & von Eynatten, H. (2009). Rutile crystals as potential trace element and isotope mineral standards for microanalysis. *Chemical Geology*, *261*(3–4), 346–369. https://doi.org/10.1016/j.chemgeo.2008.04.012

Marschall, H. R., Dohmen, R., & Ludwig, T. (2013). Diffusion-induced fractionation of niobium and tantalum during continental crust formation. *Earth and Planetary Science Letters*, *375*, 361–371. https://doi.org/10.1016/j.epsl.2013.05.055

Martinez, R. B. (2015). Avaliação de métodos para cálculo e inferência de condições P-T em rochas da fácies granulito: investigação das rochas das Nappes Três Pontas-Varginha e Socorro-Guaxupé. 161.

Montel, J. M., Kornprobst, J., & Vielzeuf, D. (2000). Preservation of old U-Th-Pb ages in shielded monazite: Example from the Beni Bousera Hercynian kinzigites (Morocco). *Journal of Metamorphic Geology*, *18*(3), 335–342. https://doi.org/10.1046/j.1525-1314.2000.00261.x

Moraes, R., Brown, R., Fuck, R. A., Camargo, M. A., & Lima, T. M. (2002). Characterization and P-T Evolution of Melt-bearing Ultrahigh-temperature Granulites: An Example from the Anapolis-Itaucu Complex of the Brasilia Fold Belt, Brazil. *Journal of Petrology*, *43*(9), 1673–1705. https://doi.org/10.1093/petrology/43.9.1673

Müller, A., Lennox, P., & Trzebski, R. (2002). Cathodoluminescence and micro-structural evidence for crystallisation and deformation processes of granites in the Eastern Lachlan Fold Belt (SE Australia). *Contributions to Mineralogy and Petrology*, *143*, 510–524. https://doi.org/10.1007/s00410-002-0361-x

Nachlas, W. O., & Hirth, G. (2015). Experimental constraints on the role of dynamic recrystallization on resetting the Ti-in-quartz thermobarometer. *Journal of Geophysical Research: Solid Earth*, *120*, 8120–8137. https://doi.org/10.1002/2015JB012274. Received

O'Brien, P. J. (2008). Challenges in high-pressure granulite metamorphism in the era of pseudosections: Reaction textures, compositional zoning and tectonic interpretation with examples from the Bohemian Massif. *Journal of Metamorphic Geology*, *26*(2), 235–251. https://doi.org/10.1111/j.1525-1314.2007.00758.x

O'Brien, P. J., & Rötzler, J. (2003). High-pressure granulites: Formation, recovery of peak conditions and implications for tectonics. *Journal of Metamorphic Geology*, *21*(1), 3–20. https://doi.org/10.1046/j.1525-1314.2003.00420.x

Pape, J., Mezger, K., & Robyr, M. (2016). A systematic evaluation of the Zr-in-rutile thermometer in ultra-high temperature (UHT) rocks. *Contributions to Mineralogy and Petrology*, *171*(5), 1–20. https://doi.org/10.1007/s00410-016-1254-8

Pauly, J., Marschal, H. R., Meyer, H. P., Chatterjee, N., & Monteleone, B. (2016). Prolonged ediacaran-cambrian metamorphic history and short-lived high-pressure granulitefacies metamorphism in the h.u. sverdrupfjella, dronning maud land (east antarctica): Evidence for continental collision during gondwana assembly. *Journal of Petrology*, *57*(1), 185–227. https://doi.org/10.1093/petrology/egw005

Pearce, M. A., White, A. J. R., & Gazley, M. F. (2015). TCInvestigator: Automated calculation of mineral mode and composition contours for thermocalc pseudosections. *Journal of Metamorphic Geology*, *33*(4), 413–425. https://doi.org/10.1111/jmg.12126

Pimentel, M. M. (2016). The tectonic evolution of the Neoproterozoic Brasília Belt, central Brazil: A geochronological and isotopic approach. *Brazilian Journal of Geology*, *46*(June), 67–82. https://doi.org/10.1590/2317-4889201620150004

Piuzana, D., Pimentel, M. M., Fuck, R. A., & Armstrong, R. (2003a). Neoproterozoic granulite facies metamorphism and coeval granitic magmatism in the Brasilia Belt, Central Brazil: Regional implications of new SHRIMP U – Pb and Sm – Nd data.

Precambrian Research, *125*, 245–273. https://doi.org/10.1016/S0301-9268(03)00108-6

Piuzana, D., Pimentel, M. M., Fuck, R. A., & Armstrong, R. (2003b). SHRIMP U-Pb and Sm-Nd data for the Araxá Group and associated magmatic rocks: Constraints for the age of sedimentation and geodynamic context of the southern Brasília Belt, central Brazil. *Precambrian Research*, *125*(1–2), 139–160. https://doi.org/10.1016/S0301-9268(03)00107-4

Powell, R., Holland, T., & Worley, B. (1998). Calculating phase diagrams involving solid solutions via non-linear equations, with examples using THERMOCALC. *Journal of Metamorphic Geology*, *16*, 577–588. https://doi.org/10.1111/j.1525-1314.1998.00157.x

Powell, R., & Holland, T. J. B. (1988). An internally consistent dataset with uncertainties and correlations: 3. Applications to geobarometry, worked examples and a computer program. *Journal of Metamorphic Geology*, *6*(2), 173–204. https://doi.org/10.1111/j.1525-1314.1988.tb00415.x

Prent, A. M., Beinlich, A., Morrissey, L. J., Raimondo, T., Clark, C., & Putnis, A. (2019). Monazite as a monitor for melt-rock interaction during cooling and exhumation. *Journal of Metamorphic Geology*, *37*(3), 415–438. https://doi.org/10.1111/jmg.12471

Reno, B. L., Piccoli, P. M., Brown, M., & Trouw, R. A. J. (2012). In situ monazite (U-Th)-Pb ages from the Southern Brasília Belt, Brazil: Constraints on the high-temperature retrograde evolution of HP granulites. *Journal of Metamorphic Geology*, *30*(1), 81–112. https://doi.org/10.1111/j.1525-1314.2011.00957.x

Reno, B. L., Brown, M., Kobayashi, K., Nakamura, E., Piccoli, P. M., & Trouw, R. A. (2009). Eclogite – high-pressure granulite metamorphism records early collision in West Brasília Belt, Brazil Gondwana: New data from the Southern, Brazil. *Journal of the Geological Society*, *166*, 1013–1032. https://doi.org/10.1144/0016-76492008-140.Eclogite

Rocha, B. C., Moraes, R., Möller, A., Ciof, C. R., & Jercinovic, M. J. (2017). Timing of anatexis and melt crystallization in the Socorro – Guaxupé Nappe, SE Brazil: Insights from trace element composition of zircon, monazite and garnet coupled to U — Pb geochronology. *Lithos*, *277*, 337–355. https://doi.org/10.1016/j.lithos.2016.05.020

Rubatto, D., Chakraborty, S., & Dasgupta, S. (2013). Timescales of crustal melting in the Higher Himalayan Crystallines (Sikkim, Eastern Himalaya) inferred from trace element-constrained monazite and zircon chronology. *Contributions to Mineralogy and Petrology*, *165*(2), 349–372. https://doi.org/10.1007/s00410-012-0812-y

Seer, H. J., Brod, A., Fuck, R. A., Pimentel, M. M., Boaventura, G. R., & Dardenne, M. a. (2001). Grupo Araxá em sua área tipo: Um fragmento de crosta oceânica neoproterozóica na faixa de dobramentos Brasília. *Revista Brasileira de Geociencias*, *31*(3), 385–396. https://doi.org/10.25249/0375-7536.2001313385396

Seer, H. J., & Dardenne, M. A. (2000). Tectonostratigraphic terrane analysis on neoproterozoic times: The case study of Araxá Synform, Minas Gerais state, Brazil: Implications to the final collage of the Gondwanaland. *Revista Brasileira de Geociencias*, *30*(1), 78–81. https://doi.org/10.25249/0375-7536.2000301078081

Simões, L. S. A. (1995). *Evolução tectono-metamórfica da nappe de Passos, sudoeste de Minas Gerais*. Universidade de São Paulo.

Sizova, E., Gerya, T., & Brown, M. (2014). Contrasting styles of Phanerozoic and Precambrian continental collision. *Gondwana Research*, *25*(2), 522–545. https://doi.org/10.1016/j.gr.2012.12.011

Spear, F. S., & Parrish, R. R. (1996). Petrology and cooling rates of the Valhalla complex, British Columbia, Canada. *Journal of Petrology*, *37*(4), 733–765. https://doi.org/10.1093/petrology/37.4.733

Spencer, C. J., Hawkesworth, C., Cawood, P. A., & Dhuime, B. (2013). Not all supercontinents are created equal: Gondwana-rodinia case study. *Geology*, *41*(7), 795–798. https://doi.org/10.1130/G34520.1

Taylor-Jones, K., & Powell, R. (2015). Interpreting zirconium-in-rutile thermometric results. *Journal of Metamorphic Geology*, *33*(2), 115–122. https://doi.org/10.1111/jmg.12109

Tedeschi, M., Lanari, P., Rubatto, D., Pedrosa-Soares, A., Hermann, J., Dussin, I., Pinheiro, M. A. P., Bouvier, A. S., & Baumgartner, L. (2017). Reconstruction of multiple P-T-t stages from retrogressed mafic rocks: Subduction versus collision in the Southern Brasília orogen (SE Brazil). *Lithos*, *294–295*, 283–303. https://doi.org/10.1016/j.lithos.2017.09.025

Tedeschi, M., Pedrosa-Soares, A., Dussin, I., Lanari, P., Novo, T., Pinheiro, M. A. P., Lana, C., & Peters, D. (2018). Protracted zircon geochronological record of UHT garnet-free granulites in the Southern Brasília orogen (SE Brazil): Petrochronological constraints on magmatism and metamorphism. *Precambrian Research*, *316*(December 2017), 103–126. https://doi.org/10.1016/j.precamres.2018.07.023

Thomas, J. B., Watson, E. B., Spear, F. S., Shemella, P. T., Nayak, S. K., & Lanzirotti, A. (2010). TitaniQ under pressure: The effect of pressure and temperature on the solubility of Ti in quartz. *Contributions to Mineralogy and Petrology*, *160*(5), 743–759. https://doi.org/10.1007/s00410-010-0505-3

Thomas, J. B., Watson, E. B., Spear, F. S., & Wark, D. A. (2015). TitaniQ recrystallized: Experimental confirmation of the original Ti-in-quartz calibrations. *Contributions to Mineralogy and Petrology*, *169*(3), 27. https://doi.org/10.1007/s00410-015-1120-0

Tiwari, S. K., & Biswal, T. K. (2019). Dynamics, EPMA Th-U-Total Pb Monazite Geochronology and Tectonic Implications of Deformational Fabric in the Lower-Middle Crustal Rocks: A Case Study of Ambaji Granulite, NW India. *Tectonics*, *38*(7), 2232–2254. https://doi.org/10.1029/2017TC004891

Tomkins, H. S., Powell, R., & Ellis, D. J. (2007). The pressure dependence of the zirconium-in-rutile thermometer. *Journal of Metamorphic Geology*, *25*(6), 703–713. https://doi.org/10.1111/j.1525-1314.2007.00724.x

Trouw, R. A. J. (1992). Evolução tectônica ao sul do cráton de São Francisco, baseada em análise metamórfica. Boletim de Resumos Expandidos Do XXXVII Congresso Brasileiro de Geologia, 327.

Trouw, R. A. J., Heilbron, M., Ribeiro, A., Paciullo, F. V. P., Valeriano, C. M., Almeida, J. C. H., Tupinambá, M., & Andreis, R. R. (2000). The Central Segment of the Ribeira Belt. In U. G. Cordani, E. J. Milani, A. Thomaz Filho, & D. A. Campos (Eds.), *Tectonic Evolution of South America* (1st ed.) (pp. 287–310). COMPANHIA DE PESQUISA DE RECURSOS MINERAIS.

Trouw, Rudolph A J, Paciullo, F. V. P., & Heilbron, M. (1984). Os Grupos São João Del Rei, Carrancas e Andrelândia

Interpretados como a Continuição dos Grupos Araxá e Canastra. *Anais Do XXXIII Congresso Brasileiro de Geologia*, 177–178.

Trouw, R. A. J., Peternel, R., Ribeiro, A., Heilbron, M., Vinagre, R., Duffles, P., Trouw, C. C., Fontainha, M., & Kussama, H. H. (2013). A new interpretation for the interference zone between the southern Brasília belt and the central Ribeira belt, SE Brazil. *Journal of South American Earth Sciences*, 48, 43–57. https://doi.org/10.1016/j.jsames.2013.07.012

Valeriano, C. M. (2017). The Southern Brasília Belt. In M. Heilbron, U. G. Cordani, & F. Alkmim (Eds.), *São Francisco Craton, Eastern Brazil. Regional Geology Reviews* (pp. 189–203). Springer International Publishing. https://doi.org/10.1007/978-3-319-01715-0

Valeriano, C. M., Dardene, M. A., Fonseca, M. A., Simões, L. S. A., & Seer, H. J. (2004). A evolução Tectônica da Faixa Brasília. In V. Mantesso Neto, A. Bartorelli, C. D. R. Carneiro, & B. B. de Brito Neves (Eds.), *Geologia do Continente sul-americano: evolução da obra de Fernando Flávio Marques de Almeida* (pp. 575–592). Beca Ed.

Valeriano, C. M., Machado, N., Simonetti, A., Valladares, C. S., Seer, H. J., & Simões, L. S. A. (2004). U – Pb geochronology of the southern Brasília nelt (SE-Brazil): sedimentary provenance, Neoproterozoic orogeny and assembly of West Gondwana. *Precambrian Research*, 130, 27–55. https://doi.org/10.1016/j.precamres.2003.10.014

Valeriano, C. M., & Simões, L. S. A. (1997). Geochemistry of Proterozoic mafic rocks from the Passos Nappe (Minas Gerais, Brazil): tectonic implications to the evolution of the southern Brasilia belt. *Brazilian Journal of Geology*, 27(1), 99–110.

Valeriano, C. M., Teixeira, W., Heilbron, M., & Simões, L. S. A. (2000). Southern Brasília Belt (SE Brazil): Tectonic Discontinuities, K-Ar data and Evolution during the Neoproterozoic Brasiliano Orogeny. *Revista Brasileira de Geociencias*, 30(1), 195–199. https://doi.org/10.25249/0375-7536.2000301195199

Valeriano, C. M., Pimentel, M. M., Heilbron, M., Almeida, J. C. H., & Trouw, R. A. J. (2008). Tectonic evolution of the Brasília Belt, Central Brazil, and early assembly of Gondwana. *Geological Society Special Publication*, 294, 197–210. https://doi.org/10.1144/SP294.11

Vlach, S. R. F. (2010). Th-U-PbT dating by electron probe microanalysis, part I. Monazite: analytical procedures and data treatment. *Geologia USP: Série Científica*, 10(1), 61–85. https://doi.org/10.5327/Z1519-874X2010000100006

Westin, A., Campos Neto, M. C., Hollanda, M. H. B. M., Salazar-Mora, C. A., Queiroga, G. N., Frugis, G. L., & de Castro, M. P. (2021). The fast exhumation pattern of a Neoproterozoic nappe system built during West Gondwana amalgamation: Insights from thermochronology. *Precambrian Research*, 355(February), 106115. https://doi.org/10.1016/j.precamres.2021.106115

White, R. W., Powell, R., & Halpin, J. A. (2004). Spatially-focussed melt formation in aluminous metapelites from Broken Hill, Australia. *Journal of Metamorphic Geology*, 22(9), 825–845. https://doi.org/10.1111/j.1525-1314.2004.00553.x

White, R. W., Powell, R., Holland, T. J. B., Johnson, T. E., & Green, E. C. R. (2014). New mineral activity-composition relations for thermodynamic calculations in metapelitic systems. *Journal of Metamorphic Geology*, 32(3), 261–286. https://doi.org/10.1111/jmg.12071

Williams, M. L., Jercinovic, M. J., Goncalves, P., & Mahan, K. (2006). Format and philosophy for collecting, compiling, and reporting microprobe monazite ages. *Chemical Geology*, 225(1–2), 1–15. https://doi.org/10.1016/j.chemgeo.2005.07.024

Williams, M. L., Jercinovic, M. J., & Hetherington, C. J. (2007). Microprobe monazite geochronology: Understanding geologic processes by integrating composition and chronology. *Annual Review of Earth and Planetary Sciences*, 35, 137–175. https://doi.org/10.1146/annurev.earth.35.031306.140228

Williams, M. L., Jercinovic, M. J., Mahan, K. H., & Dumond, G. (2017). Electron Microprobe Petrochronology. *Reviews in Mineralogy and Geochemistry*, 83(1), 153–182. https://doi.org/10.2138/rmg.2017.83.5

Zack, T., & Kooijman, E. (2017). Petrology and Geochronology of Rutile. *Reviews in Mineralogy & Geochemistry*, 83, 443–467. https://doi.org/10.2138/rmg.2017.83.14

Zack, T., Stockli, D. F., Luvizotto, G. L., Barth, M. G., Belousova, E., Wolfe, M. R., & Hinton, R. W. (2011). In situ U-Pb rutile dating by LA-ICP-MS: 208Pb correction and prospects for geological applications. *Contributions to Mineralogy and Petrology*, 162(3), 515–530. https://doi.org/10.1007/s00410-011-0609-4

SUPPORTING INFORMATION

Additional supporting information may be found in the online version of the article at the publisher's website.

Table S1: Microprobe mineral compositions of garnet, plagioclase and biotite from samples SSPDH10, SSPDH12, MG161 and SSPDH2. Garnet formulae were calculated using 12 oxygens, plagioclase with 8 and biotite with 11.

Table S2: Trace element composition of analyzed rutile grains. RSE: Relative standard errors from counting statistics (2 sigma), only shown for analyses above detection limit. BD: values below detection limit. Temperatures are calculated after the calibration of Tomkins et al. (2007).

Table S3: Ti-in-quartz content in granulite samples. RSE: Relative standard errors from counting statistics (2 sigma), only shown for analyses above detection limit. Temperatures are calculated after the calibration of Thomas et al. (2010) and using an estimate pressure of 0.7 GPa and 1.2 GPa. *: analyses perfomed in the LA-ICP-MS, and analyses without the * were performed in the EPMA.

Table S4: Summary of whole rock composition of the studied samples. XRF: X-ray fluorescence, QCM: quantitative compositional mapping. * QCM removing the garnet core area from the quantitative map. ** QCM removing the garnet core area from the quantitative map

plus melt integrated. *** QCM role area from the quantitative map for sample plus melt integrated. Values in mol %.

Table S5: EPMA monazite major and trace element composition (values are in element %wt) and corrected concentrations of Th, U and Pb (in μg/g) and calculated ages (Ma) for the analyzed monazite. Meas: measured, 2Sig: 2 sigma error. Detection limits are those presented in Table 1. BD: bellow detection limit.

Table S6: Rutile dating data from samples SSPDH12, MG161 and SSPDH10. 1 s: 1 sigma error. Values in μg/g.

Figure S1: Mineral compositional maps for sample SSPDH12. a) Mineral distribution map from sample SSPDH12. b-e) Almandine, pyrope, grossular and spessartine zoning in garnet, respectively (where $X_{Alm} = Fe/(Fe + Ca + Mg + Mn)$, $X_{Py} = Mg/(Fe + Ca + Mg + Mn)$, $X_{Grs} = Ca/(Fe + Ca + Mg + Mn)$ and $X_{sps} = Mn/(Fe + Ca + Mg + Mn))$.

Figure S2: Standardization graphs from the compositional maps obtained from the cathodoluminescence maps and Ti-in-quartz composition.

Figure S3: Garnet isomodes. a) Garnet isomodes in the $P–T$ pseudosection calculated by removing the garnet core area from the quantitative map for sample SSPDH10. b) Garnet isomodes in a melt-reintegrated $P–T$ pseudosection calculated by including the previously excluded garnet composition for sample SSPDH10. c) Garnet isomodes in the $P–T$ pseudosection calculated by removing the garnet core area from the quantitative map for sample SSPDH2. d) Garnet isomodes in melt-reintegrated $P–T$ pseudosection calculated by including the previously excluded garnet composition for sample SSPDH2. Calculated mineral compositions for samples SSPDH10 and SSPDH2 can be found on Figure 4.

Figure S4: Kyanite isomodes. a) Kyanite isomodes in the $P–T$ pseudosection calculated by removing the garnet core area from the quantitative map for sample SSPDH10. b) Kyanite isomodes in melt-reintegrated $P–T$ pseudosection calculated by including the previously excluded garnet composition for sample SSPDH2. c) Kyanite isomodes in the $P–T$ pseudosection calculated by removing the garnet core area from the quantitative map for sample SSPDH2. e) Calculated mineral compositions for samples SSPDH10 and SSPDH2 can be found on Figure 10.

Figure S5: Biotite and rutile isomodes. a) Biotite isomodes in the $P–T$ pseudosection calculated by removing the garnet core area from the quantitative map for sample SSPDH10. b) Biotite isomodes in melt-reintegrated $P–T$ pseudosection calculated by including the previously excluded garnet composition for sample SSPDH10. c) Rutile isomodes in the P–T pseudosection calculated by removing the garnet core area from the quantitative map for sample SSPDH10. d) Rutile isomodes in Melt-reintegrated $P–T$ pseudosection calculated by including the previously excluded garnet composition for sample SSPDH10. e) Biotite isomodes in the $P–T$ pseudosection calculated by removing the garnet core area from the quantitative map for sample SSPDH2. f) Biotite isomodes in melt-reintegrated $P–T$ pseudosection calculated by including the previously excluded garnet composition for sample SSPDH2. g) Rutile isomodes in the $P–T$ pseudosection calculated by removing the garnet core area from the quantitative map for sample SSPDH2. h) Rutile isomodes in melt-reintegrated $P–T$ pseudosection calculated by including the previously excluded garnet composition for sample SSPDH2. Calculated mineral compositions for samples SSPDH10 and SSPDH2 can be found on Figure 10.